

# Experimental robustness benchmark of quantum neural network on a superconducting quantum processor

Hai-Feng Zhang,<sup>1</sup> Zhao-Yun Chen,<sup>2,\*</sup> Peng Wang,<sup>1</sup> Liang-Liang Guo,<sup>1</sup> Tian-Le Wang,<sup>1</sup> Xiao-Yan Yang,<sup>1</sup> Ren-Ze Zhao,<sup>1</sup> Ze-An Zhao,<sup>1</sup> Sheng Zhang,<sup>1</sup> Lei Du,<sup>1</sup> Hao-Ran Tao,<sup>1</sup> Zhi-Long Jia,<sup>3</sup> Wei-Cheng Kong,<sup>3</sup> Huan-Yu Liu,<sup>1</sup> Athanasios V. Vasilakos,<sup>4</sup> Yang Yang,<sup>2,5</sup> Yu-Chun Wu,<sup>1,2</sup> Ji Guan,<sup>6,†</sup> Peng Duan,<sup>1,†</sup> and Guo-Ping Guo<sup>1,§</sup>

<sup>1</sup>Laboratory of Quantum Information, School of Physics, University of Science and Technology of China, Hefei, Anhui, 230026, P. R. China

<sup>2</sup>Institute of Artificial Intelligence, Hefei Comprehensive National Science Center, Hefei, Anhui, 230088, P. R. China

<sup>3</sup>Origin Quantum Computing, Hefei, Anhui, 230026, P. R. China

<sup>4</sup>Department of ICT and Center for AI Research, University of Agder (UiA), Jon Lilletuns vei 9, 4879 Grimstad, Norway

<sup>5</sup>Anhui University, Hefei, Anhui, 230039, P. R. China

<sup>6</sup>Key Laboratory of System Software (Chinese Academy of Sciences) and State Key Laboratory of Computer Science, Institute of Software, Chinese Academy of Sciences, Beijing 100190, P. R. China

Quantum machine learning (QML) models, like their classical counterparts, are vulnerable to adversarial attacks, hindering their secure deployment. Here, we report the first systematic experimental robustness benchmark for 20-qubit quantum neural network (QNN) classifiers executed on a superconducting processor. Our benchmarking framework features an efficient adversarial attack algorithm designed for QNNs, enabling quantitative characterization of adversarial robustness and robustness bounds. From our analysis, we verify that adversarial training reduces sensitivity to targeted perturbations by regularizing input gradients, significantly enhancing QNN's robustness. Additionally, our analysis reveals that QNNs exhibit superior adversarial robustness compared to classical neural networks, an advantage attributed to inherent quantum noise. Furthermore, the empirical upper bound extracted from our attack experiments shows a minimal deviation ( $3 \times 10^{-3}$ ) from the theoretical lower bound, providing strong experimental confirmation of the attack's effectiveness and the tightness of fidelity-based robustness bounds. This work establishes a critical experimental framework for assessing and improving quantum adversarial robustness, paving the way for secure and reliable QML applications.

Over the past decade, machine learning (ML), particularly deep neural networks, has become indispensable to critical applications ranging from natural language processing to autonomous driving [1, 2]. However, the widespread deployment of these models has concurrently brought their security vulnerabilities to the forefront. A pressing concern is their susceptibility to adversarial attacks—carefully crafted, often imperceptible input perturbations that can induce misclassification or erroneous behavior, posing risks in sensitive applications like facial recognition [3–5]. Rigorous robustness evaluation is thus imperative for ML reliability and safety [6].

Quantum machine learning (QML) [7, 8], employing models like quantum neural networks (QNNs), seeks to leverage quantum computational principles for potential advantages in areas such as high-dimensional data analysis and complex system simulation [9–12]. Driven by advancements in quantum hardware platforms like superconducting circuits, the practical implementation and experimental investigation of QNNs are gaining significant momentum [13–20]. Despite their distinct computational paradigm, QNNs unfortunately appear to inherit vulnerabilities analogous to their classical counterparts [21, 22]. Consequently, ensuring the security and trustworthy deployment of QNNs, particularly their robustness against adversarial threats, has emerged as a critical research priority [23]. Initial theoretical work has formalized fidelity-based robustness bounds, enabling rapid evaluation of robustness for specific input samples [24, 25]. Additionally, other researchers have explored the resilience of QMLs against black-box attacks transferred from classical domains, suggesting a potential quantum robustness advantage [26].

To date, a systematic evaluation of QML's robustness on real quantum hardware remains absent from the current literature. This requires an *in-situ* implementation of effective adversarial attacks executed on quantum devices. Such an approach serves a dual purpose: it allows for the quantification of QML susceptibility to adversarial perturbations and enables the use of generated adversarial examples to assess the tightness of theoretical robustness bounds. This endeavor is experimentally formidable, however, as inherent quantum noise can obscure attack efficacy and distort robustness analyses. Consequently, quantitative validation of robustness improvements from methods like quantum adversarial training on physical systems has also remained elusive, with evaluations predominantly qualitative [27].

In this work, we present the first systematic experimental benchmark of robustness for QNNs deployed on a superconducting quantum processor. To this end, we propose an efficient adversarial attack algorithm tailored for QNNs and quantitatively characterize the model's adversarial robustness and robustness bounds under both clean and adversarial training conditions. Our analysis shows that adversarial training, through intrinsic regularization of input gradients, leads to a marked reduction in the QNN's sensitivity to adversarial perturbations, enhancing adversarial robustness by up to 179%. Comparative experiment further reveals that the QNN exhibits superior adversarial robustness compared to classical neural networks under an identical task, underscoring the robustness advantage of the quantum model attributable to quantum noise.

Additionally, we experimentally validate the fidelity-based

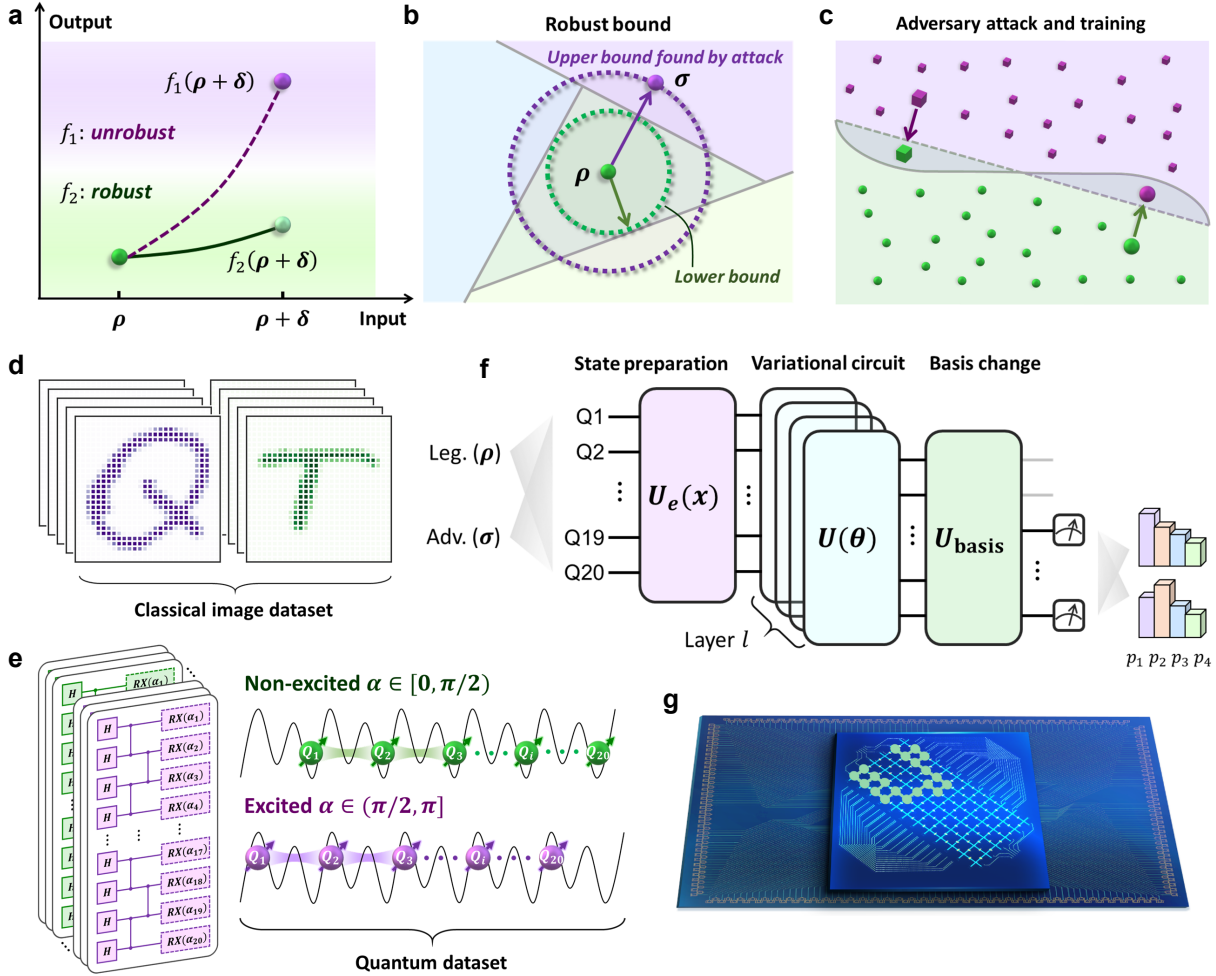


**FIG. 1. Experimental schematic for QNN robustness evaluation.** **a**, Adversarial robustness, quantified by the output sensitivity to input perturbations. **b**, Illustration of the robustness lower and upper bounds of the classifier. **c**, Schematic of adversarial attacks and adversarial training. **d**, Visualization of handwritten letters “Q” and “T” used in the image classification. **e**, Quantum circuit for generating the LCEI quantum dataset, illustrating the application of an  $R_x(\alpha)$  after the linear cluster state, with states labeled as “excited” or “non-excited” based on the rotation angle  $\alpha$ . **f**, Architecture of the QNN classifier, consisting of a state preparation circuit, an  $l$ -layer variational circuit, and pre-measurement basis transformation gates. **g**, Schematic of the superconducting quantum processor, showing 72 qubits and 126 couplers in a 2D lattice, and 20 qubits selected for the experiment are highlighted in green.

robustness lower bound for the QNN. The upper bound, empirically extracted from our attack experiments, shows only a minimal deviation (approximately  $3 \times 10^{-3}$ ) from the theoretical lower bound. This narrow gap provides strong experimental confirmation of both the tightness of the fidelity-based robustness bound and the effectiveness of our attack method. Additionally, we find that adversarial training significantly improves the mean robustness bound across all classes by more than fourfold. Our study was conducted using a state-of-the-art 20-qubit QNN with 181 trainable parameters, which achieves high-precision classification on both classical image and quantum state datasets. This work establishes a comprehensive experimental workflow for quantum adversarial attacks, defenses, and robustness evaluation, marking a pivotal milestone in QML robustness research.

## Experimental setup and framework

Our research focuses on a QNN classifier based on variational quantum circuits (VQCs) [28–30]. The architecture consists of a state preparation circuit, multilayer variational circuits, and basis transformation gates applied to the output qubits, as illustrated in Fig. 1f. The variational parameters  $\theta$  are optimized to minimize the empirical risk  $J(\theta)$ :

$$\theta^* = \arg \min_{\theta} J(\theta), \quad (1)$$

$$J(\theta) = \mathbb{E}_{(\mathbf{x}, k) \in \mathcal{D}} [\mathcal{L}(f(\mathbf{x}; \theta), k)],$$

where  $\mathcal{D}$  is training set,  $f(\mathbf{x}; \theta)$  represents the hypothesis function of the QNN classifier,  $k$  is one-hot encoding of label  $k$ , and  $\mathcal{L}$  is the cross-entropy loss applied function.

This work evaluates QNN robustness using two key metrics: adversarial robustness and robustness bound. Adversar-

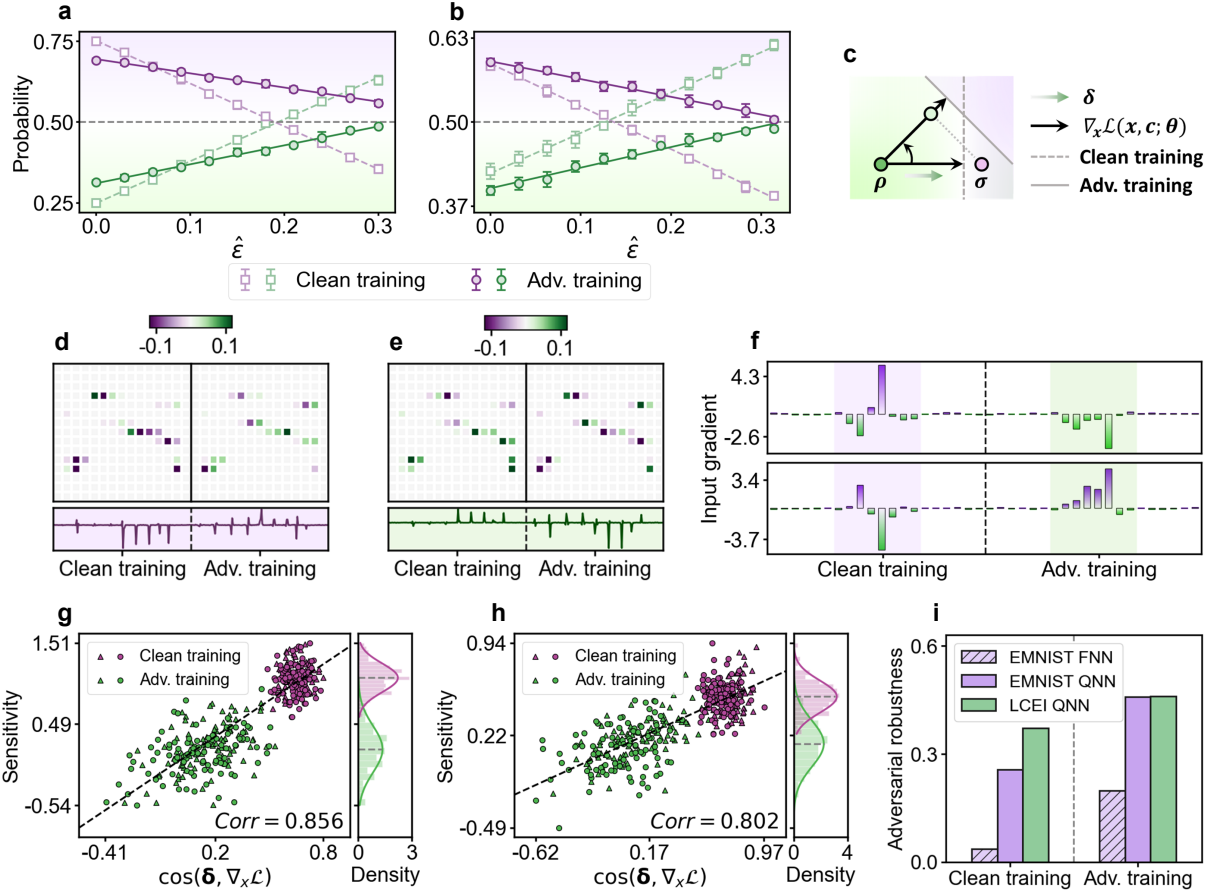


**FIG. 2. Adversary robustness benchmarking experiments.** **a, b.** QNN sensitivity experiment for EMNIST (**a**) and LCEI (**b**). Output probabilities are plotted as functions of normalized perturbation strength  $\hat{\epsilon}$ , with purple and green indicating distinct classes. Datas ( $n = 5$  independent experiments) are presented in the form of mean values  $\pm$  standard deviation (SD), with solid and dashed lines denoting linear fits for clean and adversarially trained models, respectively. **c** Diagram of the local classification landscape, illustrating how adversarial training reorients input gradients to enhance robustness. **d, e.** Comparison of average input gradients for images “Q” (**d**) and “T” (**e**). The top panels show per-pixel gradients, while the bottom panels show flattened gradient vectors. **f.** Comparison of average input gradients for LCEI states. The top panel shows the gradients of rotation angle for excited clusters, while the bottom for non-excited clusters. **g, h.** Correlation between the sensitivity and cosine similarity  $\cos(\delta, \nabla_x \mathcal{L})$  for EMNIST (**g**) and LCEI (**h**), with triangles and circles for different classes. The right panels show the sensitivity distribution under clean and adversarial training. **i.** Comparison of adversarial robustness between QNN and FNN under clean and adversarial training conditions on the same EMNIST dataset.

ial robustness is assessed by evaluating the model’s performance under specific adversarial perturbations: high sensitivity indicates poor robustness, whereas low sensitivity implies better robustness. (Fig. 1a). Robustness bounds quantify the minimum perturbation distance required to induce misclassification (Fig. 1b). These bounds can be theoretically derived (lower bounds) or empirically estimated via effective attack construction (upper bounds). To quantitatively analyze how adversarial training impacts these characteristics, we compare standard trained QNNs (clean training) with those under adversarial training. Adversarial training (Fig. 1c), a recognized defense strategy, enhances model resilience by incorporating adversarial examples into the training process.

Accurate and efficient adversarial attack algorithms are crucial for benchmarking model robustness. We propose Mask FGSM, a localized attack variant of the Fast Gradient Sign

Method (FGSM) [31], designed to enable efficient attacks and rapid generation of adversarial samples in QML experiments. It achieves this by applying perturbations only to a strategically selected sparse subset of input features, defined by a binary mask  $\mathcal{M} = (m_1, m_2, \dots, m_{\dim(x)})^T$ . This sparse perturbation strategy is adopted to minimize the computational cost of the attack and mitigate the impact of noisy gradients on attack effectiveness, especially in experimental settings. Adversarial samples are generated by perturbing legitimate samples as  $\mathbf{x}' = \mathbf{x} + \delta$ , with the perturbation components  $\delta_i$  determined based on:

$$\delta_i = \begin{cases} \epsilon \cdot \text{sgn} \left( \frac{\partial \mathcal{L}(f(\mathbf{x}; \boldsymbol{\theta}), \mathbf{c})}{\partial x_i} \Big|_{\boldsymbol{\theta}=\boldsymbol{\theta}^*} \right), & m_i = 1 \\ 0, & m_i = 0 \end{cases} \quad (2)$$

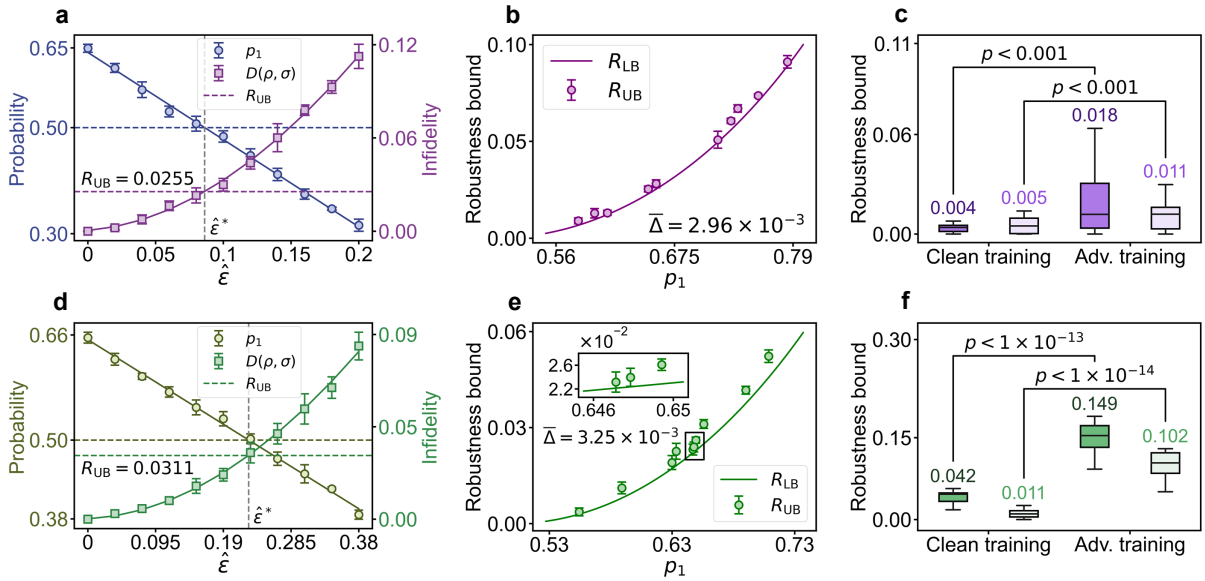


**FIG. 3. Robustness Bound validation Experiments.** **a, d.** Experiments for extracting upper bound  $R_{UB}$ , plotting predicted probabilities  $p_1$  and infidelity  $D(\rho, \sigma)$  as functions of  $\hat{\epsilon}$ . Data ( $n = 5$  independent experiments) are shown as mean  $\pm$  SD. Solid lines indicate fitting curves of  $p_1$  and  $D(\rho, \sigma)$ . Purple (a) and green (d) dashed lines mark  $R_{UB}$  extracted at  $\hat{\epsilon}^*$ . **b, e.** Comparison of the experimental upper bound  $R_{UB}$  (from 10 randomly selected samples, 5 per class) versus theoretical  $R_{LB}$ . Error bars indicate the root mean square error from fitting  $D(\rho, \sigma)$ .  $\bar{\Delta}$  denotes the average gap between  $R_{UB}$  and  $R_{LB}$  of the 10 samples. **c, f.** The robustness bounds for critical samples under clean and adversarial training. Adversarial training significantly increased the average robustness bound, with dark and light colors denoting distinct classes.  $p$ -value  $\leq 0.001$ , indicating statistically significant differences. Panels **a-c** correspond to EMNIST experiment, and **d-f** to LCEI.

where  $\epsilon$  denotes the perturbation strength. The binary mask component  $m_i$  is derived by analyzing the magnitude of input gradient components, with details provided in Methods.

Our robustness benchmarking encompasses both classical and quantum classification tasks. For the classical task, we utilize the EMNIST dataset [32] for classification of handwritten letters ‘‘Q’’ and ‘‘T’’ (Fig. 1d). The quantum task involves Linear Cluster State Excitation Identification (LCEI) [24, 33]. Using a synthetic dataset, the QNN is trained to distinguish between excited and non-excited 20-qubit cluster states, where the excitation property is determined by a rotation angle  $\alpha$  of the  $R_x$  operation applied to the end of the cluster state preparation circuit (Fig. 1e). For both binary classification tasks, predictions are based on the expectation value of the output qubit with respect to the Pauli-Z operator  $\sigma_z$ . This expectation value is mapped to a probability  $p = (\langle \sigma_z \rangle + 1)/2$ , with  $p = 0.5$  delineating the decision boundary.

Our experiment was executed on a frequency-tunable flip-chip superconducting quantum processor with 72 qubits and 126 couplers in a two-dimensional array (Fig. 1g). The characteristic transition frequencies of the couplers exceed those of the qubits, enabling dynamic tuning of effective nearest-neighbor coupling through magnetic flux biasing. For the experiment, we selected a one-dimensional (1D) array comprising 20 qubits, where arbitrary single-qubit gates and two-qubit controlled-Z (CZ) gates can be implemented for each qubit and adjacent qubit pairs. To achieve high-fidelity parallel gates, we constructed an error model to optimize the oper-

ating frequencies of all qubits and the interaction frequencies of two-qubit gates, avoiding two-level system (TLS) regions and suppressing residual coupling. See Supplementary Sections VI and VII for the device parameters and calibration details.

## Adversarial robustness

We define a measure of adversarial robustness as the average of a per-sample robustness score across the dataset, which is expressed as the inverse logistic function of sensitivity to perturbations:

$$\bar{R}_{\text{adv}} = \frac{1}{|\mathcal{D}|} \sum_{\mathbf{x} \in \mathcal{D}} \frac{1}{1 + e^{S(\mathbf{x})}}. \quad (3)$$

Here, sensitivity  $S(\mathbf{x}) = \Delta p / \hat{\epsilon}$  quantifies the impact of the input perturbation on the output, where  $\Delta p$  represents the change in the predicted probability for the correct class under a specific perturbation, and  $\hat{\epsilon} = \epsilon / (\mathbf{x}_{\text{max}} - \mathbf{x}_{\text{min}})$  as the normalized perturbation strength.

Fig. 2a, b illustrate the QNN’s sensitivity to Mask FGSM attack, plotting output probability against normalized perturbation strength for EMNIST and LCEI experiments, respectively. Clean-trained models exhibit sharp output changes under attack, leading to mispredictions, whereas adversarially trained models show significantly reduced sensitivity. This enhanced resilience stems from adversarial training regularizing the inner product of the perturbation vector  $\delta$  and the input gradient  $\nabla_{\mathbf{x}} \mathcal{L}$ . The regularization reorients the gradi-

ent to mitigate alignment with the perturbation (Fig. 2c), with a detailed proof provided in Methods. Input gradient visualizations further illustrate this phenomenon, showing distinct patterns under both training regimes for EMNIST (Fig. 2d, e) and LCEI (Fig. 2f). Notably, adversarial training preserves the critical feature regions of the inputs but modifies the magnitude of the gradient components, thereby reducing the inner product with  $\delta$ .

To statistically quantify sensitivity changes, we conducted an experiment involving 200 samples (100 per class). Fig. 2g, h show scatter plots depicting each sample's sensitivity as a function of cosine similarity,  $\cos(\delta, \nabla_x \mathcal{L})$ , for EMNIST and LCEI, respectively. The results statistically confirm that adversarial training reduces the QNN's sensitivity to target perturbations. Additionally, high Pearson correlation coefficients ( $> 0.8$ ) observed in both experiments indicate a strong correlation between sensitivity and cosine similarity, providing experimental evidence supporting the theoretical framework of input gradient regularization.

We subsequently calculated the  $\bar{R}_{\text{adv}}$  across the 200 samples. Adversarial training improved  $\bar{R}_{\text{adv}}$  from 0.256 to 0.458 for EMNIST and from 0.372 to 0.460 for LCEI, yielding up to a 179% enhancement. Fig. 2i presents a comparative analysis with a classical feedforward neural network (FNN) on EMNIST. The QNN exhibits 7.31-fold higher robustness than FNN under clean training and 2.31-fold higher under adversarial training. This quantum robustness advantage is attributed to quantum noise-induced enhancement, as detailed in Supplementary Section VI. This phenomenon is conceptually analogous to noise injection techniques used for robustness enhancement in classical neural networks [34–37]. Our results reveal the inherent superiority of the quantum model's resilience to perturbations.

## Robustness bound

Beyond these empirical metrics of adversarial robustness, a comprehensive understanding of QNN resilience requires assessing theoretical robustness guarantees. Using the Mask FGSM attack, we also experimentally validate the fidelity-based robustness lower bound for the QNN. A closed-form expression for this bound, derived from Ref. [24], is given by:

$$R_{\text{LB}} = \frac{1}{2}(\sqrt{p_1} - \sqrt{p_2})^2, \quad (4)$$

where  $p_1$  and  $p_2$  denote the predicted probabilities associated with the correct and competing classes, respectively. This lower bound guarantees correct classification if the infidelity  $D(\rho, \sigma) < R_{\text{LB}}$ . Here,  $D(\rho, \sigma) = 1 - F(\rho, \sigma)$  and  $F(\rho, \sigma) = (\text{Tr}(\sqrt{\sqrt{\rho}\sigma\sqrt{\rho}}))^2$  is the fidelity between the quantum states of output qubit, with  $\rho$  representing the state generated by the legitimate sample, and  $\sigma$  to the perturbed sample.

We then determine the upper bound  $R_{\text{UB}}$  by performing Mask FGSM attacks, measuring the  $p_1$  and infidelity  $D(\rho, \sigma)$  as a function of perturbation strength. Here,  $\rho$  and  $\sigma$  are obtained by quantum state tomography on the output qubit. We fit  $p_1$  and  $D(\rho, \sigma)$  using  $\cos^2$  functions. From the fitted curve

of  $p_1$ , we calculated the perturbation strength  $\hat{\epsilon}^*$  at the misclassification threshold ( $p_1 = 0.5$ ). Then, by inputting this  $\hat{\epsilon}^*$  value into the fitted curve of  $D(\rho, \sigma)$ , we determined the corresponding infidelity, which is defined as  $R_{\text{UB}}$ , shown in Fig. 3a, d for EMNIST and LCEI. We compare  $R_{\text{UB}}$ , determined from five randomly selected samples per class, to the theoretical  $R_{\text{LB}}$ . The results, shown in Fig. 3b, e, demonstrate that our experimental upper bounds exceed the theoretical lower bounds by average gaps of only  $2.96 \times 10^{-3}$  for EMNIST and  $3.25 \times 10^{-3}$  for LCEI. This confirms both the near-optimality of our attack and the tightness of the fidelity-based bound.

Critical samples are defined as the 20% of samples exhibiting the smallest robustness bound under clean training, representing those with lower redundancy and heightened vulnerability to attacks. Fig. 3e, f illustrate the changes in the robustness bounds for these critical samples after adversarial training. Adversarial training substantially increased the mean robustness bound of these samples by factors of 4.22 (EMNIST) and 4.74 (LCEI), demonstrating the effectiveness of adversarial training in enhancing QNN resilience and reducing misclassification risk under adversarial perturbations.

## Discussion

In summary, this work presents the first experimental benchmarking of QNN's robustness implemented on a 20-qubit superconducting quantum processor. The Mask FGSM attack algorithm effectively probes QNN vulnerabilities, and our quantitative analysis demonstrates that adversarial training enhances adversarial robustness and the robustness bound of critical samples. Comparative experiments show QNNs' superior adversarial robustness over classical neural networks under both clean and adversarial training, reflecting the robustness advantage induced from quantum noise. Future research should expand the scope of robustness evaluation to include unsupervised quantum classifiers and other QML models [7], while exploring the interplay between quantum noise and adversarial robustness in broader contexts is important and fascinating.

Despite these advances, adversarial training, while markedly improving targeted robustness, does not offer universal protection. The existence of adversarial samples is a common phenomenon in high-dimensional QML [22, 38], and quantum adversarial learning essentially patches models against known attacks. Absolute robustness for non-trivial classifiers remains unattainable, as such a model would degenerate into a constant function. In classical ML, extensive research focuses on robustness enhancement techniques, such as defensive distillation [39] and gradient regularization [40], which remain open challenges in QML. Moreover, the practical manifestation of QNN robustness advantages in real-world applications requires extensive long-term investigation. Our work takes a foundational step in this direction, establishing a comprehensive experimental framework for assessing quantum adversarial robustness and laying the groundwork for fu-

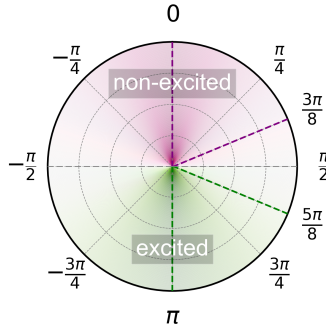


FIG. 4. **Distribution of  $\alpha$  for the synthetic quantum dataset in LCEI.** Quantum data for the two classes are sampled from  $\alpha \in [0, 3\pi/8]$  (purple dashed lines) and  $[5\pi/8, \pi]$  (green dashed lines).

ture research into the information security of general QML.

## Methods

### Training QNN classifier

Here, we detail the implementation of the two QNN classifiers investigated in this study, covering three key aspects: dataset, variational circuit, and training algorithm.

*Dataset.* For the EMNIST task, we utilized a subset of 600 handwritten letter images (“Q” and “T”, 300 each) from the EMNIST dataset, split into 500 for training and 100 for testing. Images were resized to  $15 \times 15$  resolution to balance encoding cost and classification accuracy. For LCEI, we generate a linear cluster state:

$$|\text{LC}_n\rangle = \left( \prod_{i=1}^{n-1} \text{CZ}_{i,i+1} \right) |+\rangle^{\otimes n}. \quad (5)$$

Then, an  $R_x(\alpha)$  gate is applied post-cluster state preparation, rotating qubits about the Bloch sphere’s  $x$ -axis with  $-\pi \leq \alpha \leq \pi$ . A sufficiently large rotation  $|\alpha| \in (\pi/2, \pi]$  defines an excited cluster state, while  $|\alpha| \in [0, \pi/2]$  denotes a non-excited state. We created a synthetic quantum dataset by uniformly sampling 150  $\alpha$  values from  $[0, 3\pi/8]$  and  $[5\pi/8, \pi]$  for the “non-excited” and “excited” classes, respectively (Fig. 4). From these, 200 states are randomly assigned to the training set, with 100 reserved for testing.

*Variational circuit.* We implemented a hardware-efficient variational circuit featuring interleaved layers of single- and two-qubit gates. Single-qubit SU(2) gates serve as both data encoding gates and variational parameters, while nearest-neighbor CZ gates provide entanglement within layers to reduce compilation overhead. The variational circuit, with a 40-layer gate depth and 181 trainable parameters, is employed in this work. For the high-dimensional EMNIST image data, we adopted an interleaved block encoding strategy specifically because it is known from literature [27, 41, 42] to enhance performance on image datasets, where variational parameters and features are encoded into parameterized gates via linear combinations. For LCEI, the same variational circuit is used, preceded by a cluster state preparation stage for dataset en-

coding, and detailed in Supplementary Section I.

*Training algorithm.* To optimize training efficiency and classification accuracy, we integrate mini-batch stochastic gradient descent with the Adam optimizer [43] for the training of the 20-qubit QNN classifier. Details of the training algorithm are provided in the Supplementary Section II. Clean training results (Fig. 5a, d) show optimal EMNIST accuracies of 98% (training) and 96% (test), and 100% for both in LCEI. Training accuracy reflects the classifier’s performance on mini-batches per epoch, while test accuracy denotes its performance on the test set.

### Attack Algorithm

For QML experiments, standard FGSM attacks are inefficient against high-dimensional data due to the computational overhead of input gradient calculation by parameter shift rules [44, 45]. To address this, we introduce the Mask FGSM attack, which leverages the observation that QNN classifiers exhibit consistent, localized sensitivity regions across different samples. For the EMNIST, 15% of elements in  $\mathcal{M}$  in Eq. (2) are set to 1, as our numerical results demonstrate that targeting a subset of pixels achieves attack efficacy comparable to full-pixel attacks. For the LCEI, we add perturbative angles on the  $R_x$  gates of a localized 8 qubits to generate adversarial quantum states. See Supplementary Section III for the details of Mask FGSM. Compared to standard methods, the Mask FGSM attack maintains attack effectiveness while markedly boosting efficiency. Fig. 5c, f illustrate adversarial example generation for EMNIST and LCEI, plotting accuracy as a function of the normalized perturbation strength.

### Adversarial training

We employed the Mask FGSM attack to generate 200 adversarial samples (100 per class) for EMNIST and LCEI, which were subsequently used for adversarial training. Specifically, in each training epoch, mini-batches comprise 50% legitimate samples randomly selected from the original dataset and 50% adversarial samples from the generated set. The adversarial training process is depicted in Fig. 5b, e. Following adversarial training, accuracies on the EMNIST dataset for legitimate and adversarial samples are 88% and 87%, respectively, while LCEI achieves 100% for both. To understand how adversarial training enhances robustness, we express the empirical risk in adversarial training as:

$$\tilde{\mathcal{J}}(\boldsymbol{\theta}) = \mathbb{E}_{(\mathbf{x}, k) \in \mathcal{D}} \left[ \frac{1}{2} \mathcal{L}(\mathbf{x}, \mathbf{c}; \boldsymbol{\theta}) + \frac{1}{2} \mathcal{L}(\mathbf{x} + \boldsymbol{\delta}, \mathbf{c}; \boldsymbol{\theta}) \right]. \quad (6)$$

For small perturbations  $\boldsymbol{\delta}$ , we can perform the first-order Taylor expansion of  $\mathcal{L}(\mathbf{x} + \boldsymbol{\delta}, \mathbf{c}; \boldsymbol{\theta})$  as:

$$\begin{aligned} \mathcal{L}(\mathbf{x} + \boldsymbol{\delta}, \mathbf{c}; \boldsymbol{\theta}) &= \mathcal{L}(\mathbf{x}, \mathbf{c}; \boldsymbol{\theta}) + \nabla_{\mathbf{x}} \mathcal{L}(\mathbf{x}, \mathbf{c}; \boldsymbol{\theta}) \cdot \boldsymbol{\delta} \\ &\quad + O(\boldsymbol{\delta}^2). \end{aligned} \quad (7)$$

Therefore,

$$\begin{aligned} \tilde{\mathcal{J}}(\boldsymbol{\theta}) &\approx \mathbb{E}_{(\mathbf{x}, k) \in \mathcal{D}} [\mathcal{L}(\mathbf{x}, \mathbf{c}; \boldsymbol{\theta}), \mathbf{c}] + \mathcal{R}, \\ \mathcal{R} &= \frac{1}{2} \nabla_{\mathbf{x}} \mathcal{L}(\mathbf{x}, \mathbf{c}; \boldsymbol{\theta}) \cdot \boldsymbol{\delta}. \end{aligned} \quad (8)$$

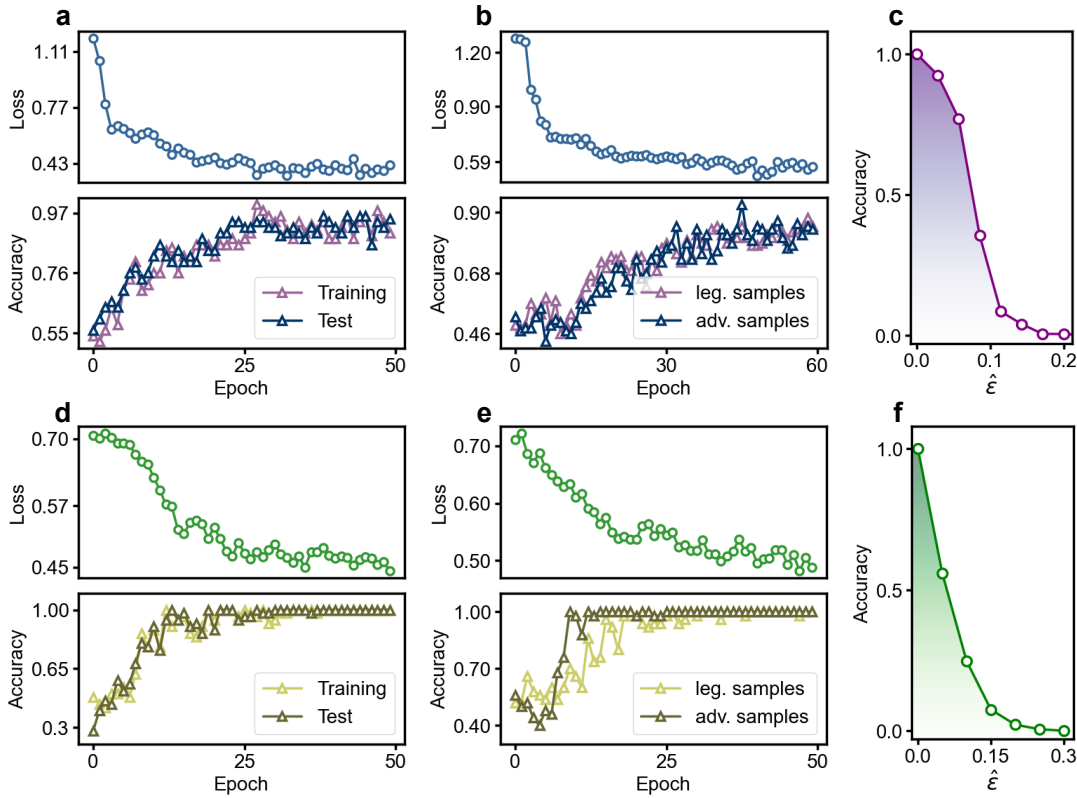


**FIG. 5. Training and attack results.** **a, d** Clean training: loss, training accuracy, and test accuracy as functions of epoch. **b, e.** Adversarial training: loss, accuracy on legitimate samples, and accuracy on adversarial samples as functions of epoch. **c, f.** Accuracy of perturbed samples under Mask FGSM attacks, plotted as functions of normalized perturbation strength. Panels **a-c** correspond to EMNIST experiment, and **d-f** to LCEI.

That is, adversarial training introduces a regularization term  $\mathcal{R}$  to the loss function, which is the inner product of the input gradient and perturbation. Minimizing this term during training encourages turning the direction of the input gradient away from the target perturbation, thereby reducing the model's sensitivity and enhancing adversarial robustness.

#### Classical neural network for comparison

To investigate the potential robustness advantage in QML, we designed a three-layer FNN to compare with QNN. The FNN consists of an input layer with 225 neurons to encode the images, a hidden layer with 5 neurons, and an output layer with a single neuron, totaling 1136 trainable parameters (weights and biases). ReLU activation functions are applied to the input and hidden layers to provide nonlinearity, while a sigmoid activation function maps the output to the interval  $[0, 1]$  for binary classification of handwritten letters. The FNN was trained using the cross-entropy loss function and the Adam optimizer with a learning rate of 0.01 over 10 epochs. We evaluated the adversarial robustness of the well-trained QNN and FNN on the same EMNIST dataset.

#### Data availability

The data that support the findings of this study are available

upon reasonable request from the authors.

#### Acknowledgements

This work has been supported by the National Key Research and Development Program of China (Grant No. 2023YFB4502500), the National Natural Science Foundation of China (Grant No. 12404564), and the Anhui Province Science and Technology Innovation (Grant No. 202423s06050001).

\* chenzhaoyun@iai.ustc.edu.cn

† guanji1992@gmail.com

‡ pengduan@ustc.edu.cn

§ gpguo@ustc.edu.cn

- [1] A. Vaswani, N. Shazeer, N. Parmar, J. Uszkoreit, L. Jones, A. N. Gomez, Ł. Kaiser, and I. Polosukhin, *Advances in neural information processing systems* **30** (2017).
- [2] P. S. Chib and P. Singh, *IEEE Transactions on Intelligent Vehicles* **9**, 103 (2023).
- [3] A. Madry, A. Makelov, L. Schmidt, D. Tsipras, and A. Vladu, *arXiv preprint arXiv:1706.06083* (2017).
- [4] Y. Zhong and W. Deng, *IEEE Transactions on Information Forensics and Security* **16**, 1452 (2021).

[5] Y. Cao, Y. Zhu, D. Wang, S. Wen, M. Xue, J. Lu, and H. Ge, arXiv preprint arXiv:2407.08514 (2024).

[6] M. Shafique, M. Naseer, T. Theocharides, C. Kyrkou, O. Mutlu, L. Orosa, and J. Choi, *IEEE Design & Test* **37**, 30 (2020).

[7] J. Biamonte, P. Wittek, N. Pancotti, P. Rebentrost, N. Wiebe, and S. Lloyd, *Quantum machine learning* (2017).

[8] M. Cerezo, G. Verdon, H.-Y. Huang, L. Cincio, and P. J. Coles, *Nature computational science* **2**, 567 (2022).

[9] S. Lloyd, M. Mohseni, and P. Rebentrost, *Nature physics* **10**, 631 (2014).

[10] P. Rebentrost, M. Mohseni, and S. Lloyd, *Physical Review Letters* **113**, [10.1103/PhysRevLett.113.130503](https://doi.org/10.1103/PhysRevLett.113.130503) (2014).

[11] V. Dunjko, J. M. Taylor, and H. J. Briegel, *Physical review letters* **117**, 130501 (2016).

[12] H.-Y. Huang, M. Broughton, J. Cotler, S. Chen, J. Li, M. Mohseni, H. Neven, R. Babbush, R. Kueng, J. Preskill, *et al.*, *Science* **376**, 1182 (2022).

[13] V. Havlíček, A. D. Córcoles, K. Temme, A. W. Harrow, A. Kandala, J. M. Chow, and J. M. Gambetta, *Nature* **567**, 209 (2019).

[14] J. Herrmann, S. M. Llima, A. Remm, P. Zapletal, N. A. McMahon, C. Scarato, F. Swiadek, C. K. Andersen, C. Hellings, S. Krinner, N. Lacroix, S. Lazar, M. Kerschbaum, D. C. Zanuz, G. J. Norris, M. J. Hartmann, A. Wallraff, and C. Eichler, *Nature Communications* **13**, [10.1038/s41467-022-31679-5](https://doi.org/10.1038/s41467-022-31679-5) (2022).

[15] M. Gong, H. L. Huang, S. Wang, C. Guo, S. Li, Y. Wu, Q. Zhu, Y. Zhao, S. Guo, H. Qian, Y. Ye, C. Zha, F. Chen, C. Ying, J. Yu, D. Fan, D. Wu, H. Su, H. Deng, H. Rong, K. Zhang, S. Cao, J. Lin, Y. Xu, L. Sun, C. Guo, N. Li, F. Liang, A. Sakurai, K. Nemoto, W. J. Munro, Y. H. Huo, C. Y. Lu, C. Z. Peng, X. Zhu, and J. W. Pan, *Science Bulletin* **68**, 906 (2023).

[16] F. Tacchino, C. Macchiavello, D. Gerace, and D. Bajoni, *npj Quantum Information* **5**, [10.1038/s41534-019-0140-4](https://doi.org/10.1038/s41534-019-0140-4) (2019).

[17] H. L. Huang, Y. Du, M. Gong, Y. Zhao, Y. Wu, C. Wang, S. Li, F. Liang, J. Lin, Y. Xu, R. Yang, T. Liu, M. H. Hsieh, H. Deng, H. Rong, C. Z. Peng, C. Y. Lu, Y. A. Chen, D. Tao, X. Zhu, and J. W. Pan, *Physical Review Applied* **16**, [10.1103/PhysRevApplied.16.024051](https://doi.org/10.1103/PhysRevApplied.16.024051) (2021).

[18] K. Huang, Z.-A. Wang, C. Song, K. Xu, H. Li, Z. Wang, Q. Guo, Z. Song, Z.-B. Liu, D. Zheng, *et al.*, *npj Quantum Information* **7**, 165 (2021).

[19] C. Zhang, Z. Lu, L. Zhao, S. Xu, W. Li, K. Wang, J. Chen, Y. Wu, F. Jin, X. Zhu, *et al.*, arXiv preprint arXiv:2409.09729 (2024).

[20] J. Chen, Y. Wu, Z. Yang, S. Xu, X. Ye, D. Li, K. Wang, C. Zhang, F. Jin, X. Zhu, *et al.*, arXiv preprint arXiv:2503.11047 (2025).

[21] S. Lu, L. M. Duan, and D. L. Deng, *Physical Review Research* **2**, [10.1103/PhysRevResearch.2.033212](https://doi.org/10.1103/PhysRevResearch.2.033212) (2020).

[22] N. Liu, N. Liu, N. Liu, P. Wittek, P. Wittek, P. Wittek, and P. Wittek, *Physical Review A* **101**, [10.1103/PhysRevA.101.062331](https://doi.org/10.1103/PhysRevA.101.062331) (2020).

[23] N. Franco, A. Sakhnenko, L. Stolpmann, D. Thuerck, F. Petsch, A. Rüll, and J. M. Lorenz, in *2024 IEEE International Conference on Quantum Computing and Engineering (QCE)*, Vol. 1 (IEEE, 2024) pp. 1467–1477.

[24] J. Guan, W. Fang, and M. Ying, in *Computer Aided Verification: 33rd International Conference, CAV 2021, Virtual Event, July 20–23, 2021, Proceedings, Part I* 33 (Springer, 2021) pp. 151–174.

[25] Y. Lin, J. Guan, W. Fang, M. Ying, and Z. Su, arXiv preprint arXiv:2407.13533 (2024).

[26] M. T. West, S. M. Erfani, C. Leckie, M. Sevior, L. C. Hollenberg, and M. Usman, *Physical Review Research* **5**, [10.1103/PhysRevResearch.5.023186](https://doi.org/10.1103/PhysRevResearch.5.023186) (2023).

[27] W. Ren, W. Li, S. Xu, K. Wang, W. Jiang, F. Jin, X. Zhu, J. Chen, Z. Song, P. Zhang, H. Dong, X. Zhang, J. Deng, Y. Gao, C. Zhang, Y. Wu, B. Zhang, Q. Guo, H. Li, Z. Wang, J. Biamonte, C. Song, D. L. Deng, and H. Wang, *Nature Computational Science* **2**, 711 (2022).

[28] M. Benedetti, E. Lloyd, S. Sack, and M. Fiorentini, *Quantum science and technology* **4**, 043001 (2019).

[29] M. Cerezo, A. Arrasmith, R. Babbush, S. C. Benjamin, S. Endo, K. Fujii, J. R. McClean, K. Mitarai, X. Yuan, L. Cincio, and P. J. Coles, *Variational quantum algorithms* (2021).

[30] K. Bharti, A. Cervera-Lierta, T. H. Kyaw, T. Haug, S. Alperin-Lea, A. Anand, M. Degroote, H. Heimonen, J. S. Kottmann, T. Menke, W. K. Mok, S. Sim, L. C. Kwek, and A. Aspuru-Guzik, *Reviews of Modern Physics* **94**, [10.1103/RevModPhys.94.015004](https://doi.org/10.1103/RevModPhys.94.015004) (2022).

[31] I. J. Goodfellow, J. Shlens, and C. Szegedy, arXiv preprint arXiv:1412.6572 (2014).

[32] G. Cohen, S. Afshar, J. Tapson, and A. Van Schaik, in *2017 international joint conference on neural networks (IJCNN)* (IEEE, 2017) pp. 2921–2926.

[33] M. Broughton, G. Verdon, T. McCourt, A. J. Martinez, J. H. Yoo, S. V. Isakov, P. Massey, R. Halavati, M. Y. Niu, A. Zlokapa, *et al.*, arXiv preprint arXiv:2003.02989 (2020).

[34] Z. He, A. S. Rakin, and D. Fan, in *Proceedings of the IEEE/CVF conference on computer vision and pattern recognition* (2019) pp. 588–597.

[35] C. Qin, J. Martens, S. Gowal, D. Krishnan, K. Dvijotham, A. Fawzi, S. De, R. Stanforth, and P. Kohli, *Advances in neural information processing systems* **32** (2019).

[36] A. Liu, X. Liu, H. Yu, C. Zhang, Q. Liu, and D. Tao, *IEEE Transactions on Image Processing* **30**, 5769 (2021).

[37] N. Ye, L. Cao, L. Yang, Z. Zhang, Z. Fang, Q. Gu, and G.-Z. Yang, *Communications Engineering* **2**, 25 (2023).

[38] W. Gong and D.-L. Deng, *National Science Review* **9**, nwab130 (2022).

[39] N. Papernot, P. McDaniel, X. Wu, S. Jha, and A. Swami, in *2016 IEEE symposium on security and privacy (SP)* (IEEE, 2016) pp. 582–597.

[40] A. Ross and F. Doshi-Velez, in *Proceedings of the AAAI conference on artificial intelligence*, Vol. 32 (2018).

[41] A. Pérez-Salinas, A. Cervera-Lierta, E. Gil-Fuster, and J. I. Latorre, *Quantum* **4**, [10.22331/q-2020-02-06-226](https://doi.org/10.22331/q-2020-02-06-226) (2020).

[42] T. Haug, C. N. Self, and M. S. Kim, *Machine Learning: Science and Technology* **4**, [10.1088/2632-2153/acb0b4](https://doi.org/10.1088/2632-2153/acb0b4) (2023).

[43] D. P. Kingma and J. Ba, arXiv preprint arXiv:1412.6980 (2014).

[44] K. Mitarai, M. Negoro, M. Kitagawa, and K. Fujii, *Physical Review A* **98**, [10.1103/PhysRevA.98.032309](https://doi.org/10.1103/PhysRevA.98.032309) (2018).

[45] M. Schuld, V. Bergholm, C. Gogolin, J. Izaac, and N. Killoran, *Physical Review A* **99**, 032331 (2019).

[46] D. C. McKay, C. J. Wood, S. Sheldon, J. M. Chow, and J. M. Gambetta, *Physical Review A* **96**, 022330 (2017).

[47] M. Schuld and N. Killoran, *Physical Review Letters* **122**, [10.1103/PhysRevLett.122.040504](https://doi.org/10.1103/PhysRevLett.122.040504) (2019).

[48] D. P. Kingma and J. Ba, arXiv preprint arXiv:1412.6980 (2014).

[49] B. Nachman, M. Urbanek, W. A. de Jong, and C. W. Bauer, *npj Quantum Information* **6**, 84 (2020).

**Supplementary information for  
“Experimental robustness benchmark of quantum neural network on a superconducting quantum  
processor”**

**CONTENTS**

Quantum neural network classifier	S1
Training algorithm	S3
Mask attack algorithm	S4
Numerical simulation of local attack	S4
Experimental Mask attack	S5
Quantum robustness advantage induced by quantum noise	S7
Robustness bound of QNN classifier	S9
Quantum processor	S10
Device information	S10
Experimental setup	S10
Device control calibration	S12
Calibration procedure	S12
CZ gate calibration	S14
Readout error mitigation	S15

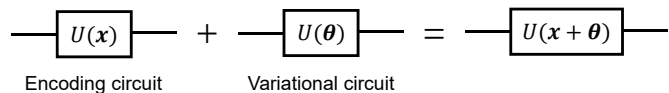
**QUANTUM NEURAL NETWORK CLASSIFIER**

The quantum neural network (QNN) classifier, denoted as  $\mathcal{A}$ , is defined by a variational quantum circuit  $U(\mathbf{x}, \boldsymbol{\theta})$  and a set of measurement operators  $\mathcal{O} = \{E_i^\dagger E_i\}$ ,  $\sum_i \mathcal{O}_i = 1$ , where the parameters  $\boldsymbol{\theta}$  are adjusted by a classical optimizer to learn a dataset  $\mathcal{D} = \{(\mathbf{x}, k_i)\}$  inputted into the circuit. The variational circuit can be written as product of  $l$ -blocks unitary  $U(\boldsymbol{\theta}) = \prod_{i=1}^l W_{\text{loc}}^{(i)}(\boldsymbol{\theta}_i) V_{\text{ent}}$ , where each block comprises of local single qubit rotations  $W_{\text{loc}}^i(\boldsymbol{\theta}_i) = \bigotimes_j R(\boldsymbol{\theta}_{i,j})$  and global entanglement operation  $V_{\text{ent}}$ . In this work, single-qubit rotations are implemented using SU(2) gate, while entanglement is provided by alternating parallel CZ gates. The SU(2) gate, offering three degrees of freedom, represents any rotation of the state vector on the Bloch sphere. It can be decomposed into hardware-adapted  $R_x(\pi/2)$  and  $R_z$  gates for execution:

$$U(\theta, \phi, \lambda) = R_z(\phi - \pi/2) R_x(\pi/2) R_z(\pi - \theta) R_x(\pi/2) R_z(\lambda - \pi/2), \quad (\text{S1})$$

where  $R_x$  ( $R_z$ ) denotes rotation about the  $X$ -( $Z$ -) axis on the Bloch sphere. The virtual Z technique is employed to implement the perfect arbitrary  $R_z$  gate [46]. The CZ gate, a common native two-bit entanglement gate on superconducting qubits, is realized by tuning qubit frequency to bring the  $|11\rangle$  and  $|20\rangle$  energy levels into resonance, with the calibration process detailed separately.

For classical datasets, such as those in image classification, data needs to be encoded into quantum states. Generally, this involves a mapping from a  $d$ -dimensional data vector to a  $2^n$ -dimensional density matrix in Hilbert space  $\mathcal{H}$  of  $n$  qubits:  $\mathbb{R}^n \rightarrow \mathbb{C}^{2^n}$ . Standard encoding schemes like basis coding, angle coding, and amplitude coding each have distinct advantages and drawbacks. However, for high-dimensional classical images, these methods typically require long encoding circuits, which are prohibitively expensive given the limited coherence times in the NISQ era. To address this, we adopt data re-uploading, also referred to as interleaved encoding, integrating the encoding circuit with the variational circuit [27, 41, 42]:



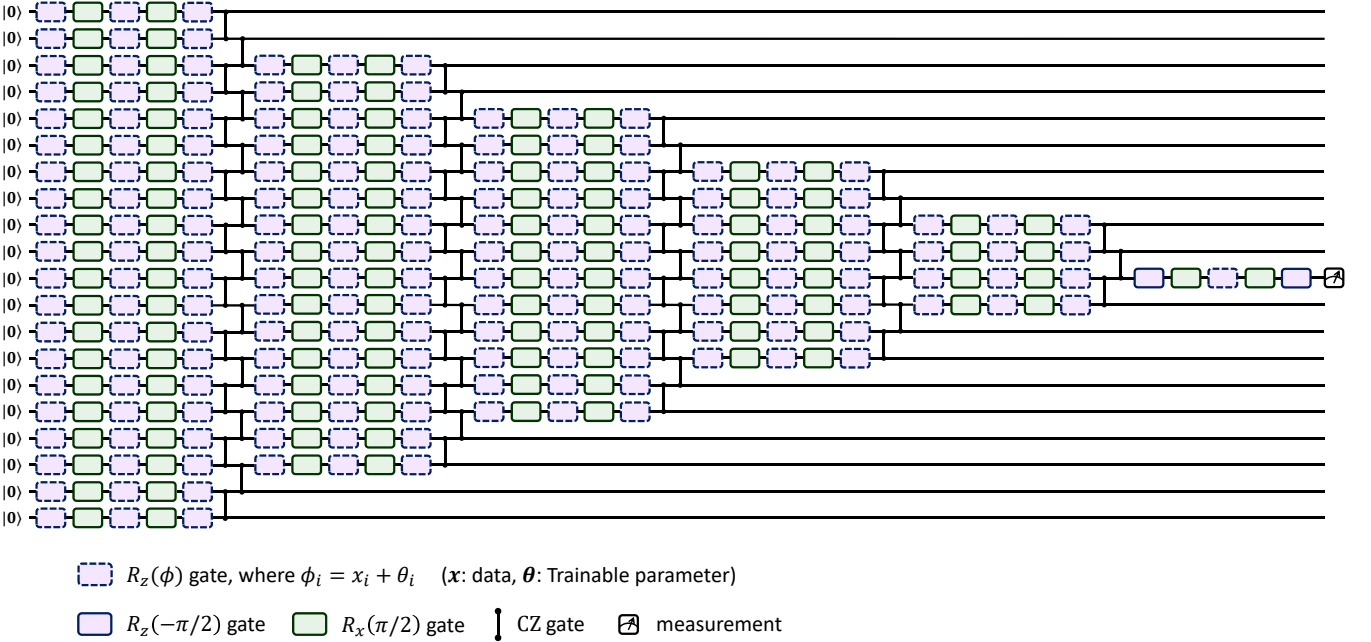


FIG. S1. **Experimental QNN circuit for classification of EMNIST dataset.** The gates with dashed violet boxes of the circuit are used both for image encoding and as a training parameter. For the  $i$ -th parametrized  $R_z$  gate,  $\phi_i = x_i + \theta_i$ , where  $x_i$  is the  $i$ -th parameter of the input encoding, and  $\theta_i$  is the  $i$ -th trainable parameter.

Implementing the interleaved encoding approach for classical images, the specific QNN circuit for the EMNIST task is illustrated in Fig. S1. This circuit features 5 blocks of decreasing size and an  $R_x$  gate before measurement, with a total of 181 trainable parameters that serve as both variational and angle encoding parameters. In order to encode the EMNIST grayscale image, we reduce the dimension of the original image to  $15 \times 15$  by quadratic interpolation, encoding only the central 169 grayscale elements, as shown in Fig. S2. The remaining 12 parameters are used solely for training and are not involved in encoding. The binary classification decision is based on measuring the middle qubit, with  $p_{|1\rangle} > 0.5$  or  $p_{|1\rangle} < 0.5$  determining the label.

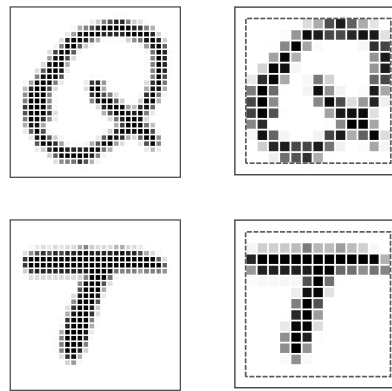


FIG. S2. **Illustration of the image preprocessing and encoding strategy for handwritten letters.** The original image (left) is downscaled to  $15 \times 15$  pixels (right), and then the valid region in the dashed box is extracted and encoded into the QNN circuit.

For the quantum cluster state excitation identification task (LCEI), The same QNN structure as classical image classification is employed. Since lacking a data encoding process, all 181 variational angles in the circuit are only trainable parameters. Instead, a state preparation circuit at the beginning of the circuit is used to input the quantum states in the target dataset.

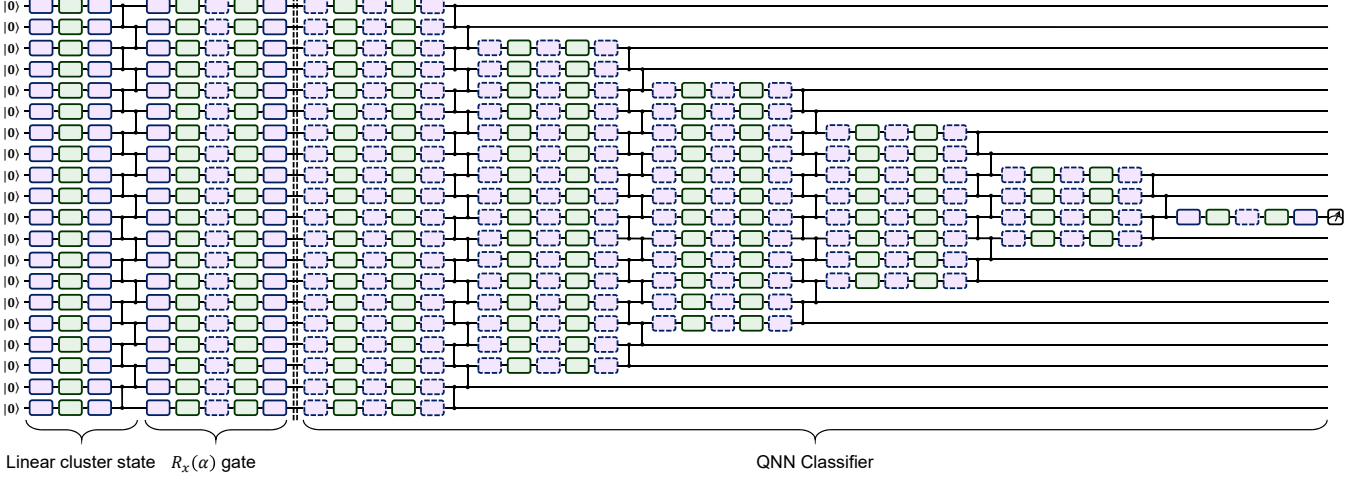


FIG. S3. **Experimental QNN circuit for LCEI.** The overall circuit scheme shares the same structure as the EMNIST circuit, with a few additional layers appended at the beginning for preparing the corresponding linear cluster state.

## TRAINING ALGORITHM

The training process of a classifier aims to minimize the empirical risk, expressed as:

$$\min_{\boldsymbol{\theta}} \frac{1}{N} \sum_{i=1}^N \sum_{k=1}^K \mathcal{L}(f(\mathbf{x}; \boldsymbol{\theta}), c_i), \quad (\text{S2})$$

given a training set of input-output pairs  $\{(\mathbf{x}_i, c_i)\}_{i=1}^N$ , where  $\boldsymbol{\theta}$  is the parameter vector of the variational circuit to be optimized, and  $\mathcal{L}$  is the loss function comparing the model output with the target label. For classification tasks, common choices include mean square error (MSE) and cross-entropy (CE) loss, with this work adopting the cross-entropy loss:

$$\mathcal{L}_{CE}(f(\mathbf{x}; \boldsymbol{\theta}), c) = \sum_{k=1}^K -c_k \log(y_k). \quad (\text{S3})$$

A typical approach for cost minimization in Eq. (S2) is the vanilla gradient descent (GD) method. In GD, parameters are updated iteratively based on the gradient of the loss to reduce the risk. At the  $t$ -th iteration, parameter  $\theta_i$  is updated as:

$$\theta_i^{(t)} = \theta_i^{(t-1)} - \eta \frac{\partial \mathcal{L}(\boldsymbol{\theta}^{(t-1)})}{\partial \theta_i} \quad (\text{S4})$$

where  $\eta$  is the learning rate. Given that the model output is related to a expected value  $\langle \mathcal{O}_k \rangle_{\boldsymbol{\theta}}$ , the partial derivative of loss function  $\frac{\partial \mathcal{L}}{\partial \theta_i}$  can be computed using the chain rule based on the derivative of the expectation value  $\frac{\partial \langle \mathcal{O}_k \rangle_{\boldsymbol{\theta}}}{\partial \theta_i}$ . For QML, an analytical gradient calculation method, the parameter-shift rule (PSR) [44, 47] is commonly employed. This enables gradient estimation on quantum hardware by executing the circuit twice, as follows:

$$\frac{\partial \langle \mathcal{O} \rangle_{\boldsymbol{\theta}}}{\partial \theta_i} = \frac{\langle \mathcal{O} \rangle_{\boldsymbol{\theta} + \frac{\pi}{2} e_i} - \langle \mathcal{O} \rangle_{\boldsymbol{\theta} - \frac{\pi}{2} e_i}}{2}, \quad (\text{S5})$$

where the subscript  $\boldsymbol{\theta} \pm \frac{\pi}{2} e_i$  denotes a parameter vector with the  $i$ -th component shifted by  $\pm \pi/2$ . The PSR is applicable to parameterized gates that are generators of Pauli operators:  $U(\theta_i) = \exp(-i \frac{\theta_i}{2} P_i)$ , where  $P_i = \{I, X, Y, Z\}^{\otimes n}$  as a tensor product of Pauli operators. Since the parameters in our variational circuit correspond to angles of single-qubit Pauli rotation gates, we can obtain the gradients using the PSR for parameter optimization.

Vanilla GD computes the gradient over the entire training dataset at each iteration. A single parameter update requires executing the circuit  $2N_p \times N_d \times N_s$  times, where  $N_d$  is the number of training data,  $N_p$  is the number of training parameters, and  $N_s$  is the number of shots required to run the circuit for estimating the measurement probabilities. This becomes computationally prohibitive for large datasets. To speed up the training process, stochastic gradient descent (SGD) or mini-batch stochastic

gradient descent (MB-SGD) is typically employed. SDG uses a single sample to evaluate the loss and compute the gradient, while MB-SGD, offering a better balance, approximates the loss gradient by randomly sampling a mini-batch subset  $B$  from the training set during each iteration. The gradient approximation and parameter update are given by:

$$\mathbf{g} \approx \frac{1}{|B|} \sum_{(\mathbf{x}_i, \mathbf{c}_i) \in B} \nabla_{\theta} \mathcal{L}(f(\mathbf{x}_i; \theta), \mathbf{c}_i), \quad (\text{S6})$$

$$\theta_t = \theta_{t-1} - \eta \mathbf{g}_t. \quad (\text{S7})$$

Notably, while MB-SGD does not provide unbiased estimates of the gradient at each step, it proves approximately effective for large-scale optimization in a noisy environment.

Although the vanilla form of MB-SGD performs well and is widely used, it faces some challenges, such as determining the learning rate without prior knowledge and the risk of converging to suboptimal local minima in non-convex objective functions. To address these, we incorporate the adaptive moment estimation (Adam) algorithm [48] into the MB-SGD. Adam is a momentum-based method featuring adaptive learning rates. The Adam update rule is defined by:

$$\mathbf{m}_t = \beta_1 \mathbf{m}_{t-1} + (1 - \beta_1) \mathbf{g}_t, \quad (\text{S8})$$

$$\mathbf{v}_t = \beta_2 \mathbf{v}_{t-1} + (1 - \beta_2) \mathbf{g}_t^2, \quad (\text{S9})$$

$$\hat{\mathbf{m}}_t = \frac{\mathbf{m}_t}{1 - \beta_1^t}, \quad (\text{S10})$$

$$\hat{\mathbf{v}}_t = \frac{\mathbf{v}_t}{1 - \beta_2^t}, \quad (\text{S11})$$

$$\theta_t = \theta_{t-1} - \eta \frac{\hat{\mathbf{m}}_t}{\sqrt{\hat{\mathbf{v}}_t} + \epsilon}. \quad (\text{S12})$$

Here,  $\mathbf{g}_t^2$  represents the Hadamard product of  $\mathbf{g}_t$  with itself.  $\mathbf{m}_t$  and  $\mathbf{v}_t$  is the first and second moment vectors, respectively.  $\epsilon$  is a small non-zero constant to prevent division by zero. Here, we refer to this optimizer, utilizing MB-SGD with Adam, as MBAdam.

For the two QNN classifiers implemented in the main text, the hyperparameters of the MBAdam are set as follows:  $\beta_1 = 0.9$ ,  $\beta_2 = 0.999$ . For EMNIST,  $\eta = 0.1$  and batch size is 100; for LCEI,  $\eta = 0.03$  and batch size is 50. These settings are kept consistent for both adversarial and clean training processes.

## MASK ATTACK ALGORITHM

### Numerical simulation of local attack

In classical adversarial learning, many algorithms for generating adversarial examples have been proposed. These methods are commonly categorized as white-box attacks or black-box attacks based on the attacker's knowledge of the target model. A well-known white-box attack method, the Fast Signed Gradient Method (FGSM), where adversarial examples  $\mathbf{x}'$  are generated from a legitimate sample  $\mathbf{x}$  according to the following formula:

$$\mathbf{x}' = \mathbf{x} + \epsilon \cdot \text{sgn}(\nabla_{\mathbf{x}} \mathcal{L}). \quad (\text{S13})$$

Here,  $\epsilon$  is the perturbation strength, and  $\nabla_{\mathbf{x}} \mathcal{L}$  is the gradient of the loss function with respect to the input  $\mathbf{x}$ . For a QNN, generating a single adversarial sample requires executing the circuit  $2N_s \times N_x$  times, where  $N_x = \dim(\mathbf{x})$ . This poses challenges for generating high-dimensional adversarial samples efficiently, particularly in batches, when gradients must be computed on quantum hardware.

To address this challenge, we consider a localized attack approach and utilize a numerical simulation experiment to illustrate the rationale behind a localized attack strategy. We conducted a numerical simulation of a QNN classifier with 12 qubits, trained on the same EMNIST dataset in the main text. The QNN adopts a circuit structure similar to that in Fig. S1. Original EMNIST images were compressed to a  $10 \times 10$  resolution for coding convenience, with an interleaved block encoding scheme applied to encode the central effective regions of these images.

We first compute input gradients for various samples (Fig. S4) on this simulated QNN, revealing that the gradient vectors are sparse and exhibit consistent sensitive regions across all samples. Then, we evaluated the QNN's vulnerability under adversarial attacks with varying sparsity levels. We incrementally increased the proportion of attacked pixels,  $r$ , starting from targeting the top 1% of pixels based on gradient magnitude, up to targeting all pixels. Fig. S5a illustrates the simulated QNN output as a

function of perturbation strength for different attack sparsity levels. Fig. S5b shows the sensitivity  $S$ , computed as a function of  $r$ . The results indicate that  $S$  saturates rapidly, with attacking approximately the top 25% of pixels achieving efficiency comparable to full-pixel attacks. Therefore, one can leverage this property to reduce gradient computation overhead, significantly reducing the required gradient computation.

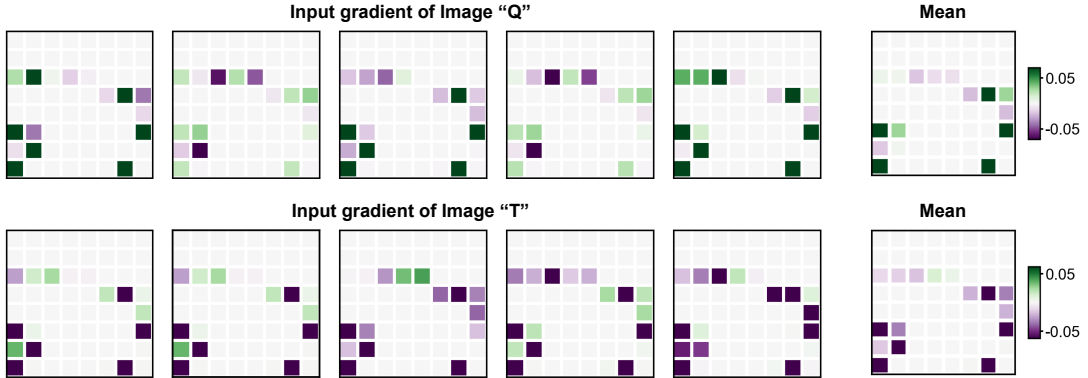
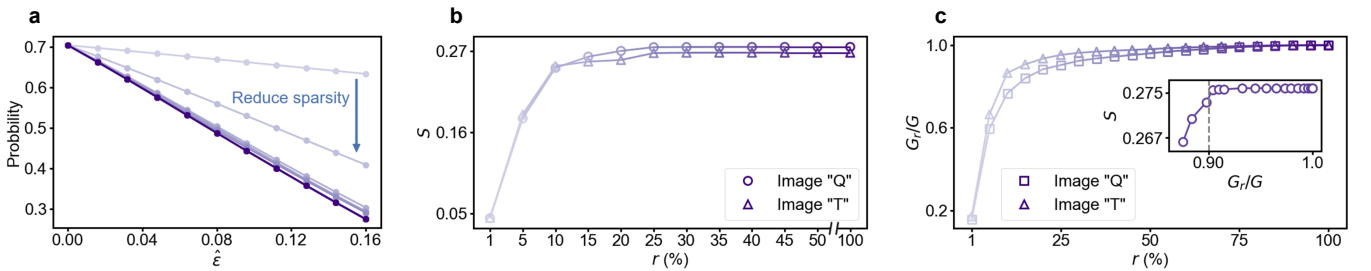


FIG. S4. **Numerical input gradients for EMNIST.** The figures show input gradients computed for five distinct handwritten letter images (“Q” and “T”), and the mean input gradient averaged across 20 different images.

To further investigate how sparsity in adversarial attacks relates to the distribution of gradient magnitudes under noise conditions, we simulated the proportion of total  $l_1$ -norm of gradient magnitude captured by the top  $r$  pixels, denoted as  $G_r/G$ , considering empirically observed measurement noise (Fig. S5c). Let  $\bar{\mathcal{G}} = (g_1, g_2, \dots, g_{N_x})^T$  be the average input gradient vector sorted in descending order of absolute component values. That is  $g_1 = \max_{i=1}^{N_x} |\partial \mathcal{L} / \partial x_i|$ , and  $g_1 > g_2 > \dots > g_{N_x}$ ,  $G_r/G$  is formally defined as:

$$\frac{G_r}{G} = \frac{\sum_{i=1}^{r \cdot N_x} |g_i|}{\|\bar{\mathcal{G}}\|_1}, \quad (\text{S14})$$

where  $\|\cdot\|_1$  denotes  $l_1$ -norm. Fig. S5c shows that  $G_r/G$  exhibits a turning point around the top 25% of pixels, after which its increase slows due to the contribution of small, noise-induced gradient components. The inset in Fig. S5c reveals the strong correlation between  $S$  and  $G_r/G$ , showing that  $S$  saturates around  $G_r/G = 0.9$ . This correlation suggests that  $G_r/G$  can serve as an effective experimental proxy for identifying the optimal subset of pixels to attack, enabling saturated attack performance with minimal computational cost.



**FIG. S5. Numerical results for local attacks with varying proportion of attacked pixels.** **a.** QNN output as a function of normalized perturbation  $\hat{\epsilon}$ . **b.** Sensitivity  $S$  under different attack proportions, computed from the data in panel **a**. **c.** Gradient magnitude proportion  $G_r/G$  as a function of pixel proportion. The inset shows  $S$  as a function of  $G_r/G$ , where  $S$  reaches saturation at 90% of the gradient components.

## Experimental Mask attack

We experimentally computed the input gradients for various samples, as shown in Fig. S6. These experimental gradients are consistent with our numerical simulation results, exhibiting similar salient gradient features across different images. Based on the sparsity observed in the experimental gradients, we propose the Mask Attack method, which utilizes a mask  $\mathcal{M}$  to determine

the localized regions to be attacked. This approach aims to minimize the number of perturbed pixels and the number of required gradient computations. Additionally, it holds the potential to mitigate the impact of noise on attack effectiveness by reducing the influence of noise on trivial gradient components. We determine the specific  $\mathcal{M}$  based on  $G_r/G$ , calculating the average input gradients of 20 samples and plotting  $G_r/G$  as a function of  $r$ , as shown in Fig. S7a. The experimental result shows that selecting the top 15% of pixels by gradient magnitude achieved  $G_r/G \approx 0.9$ . Thus,  $\mathcal{M}$  was generated by identifying the indices corresponding to the top 15% gradient components and setting the respective entries to 1, with all others being 0. Fig. S7b illustrates the  $\mathcal{M}$  used in the attack experiments on the EMNIST dataset. Algorithm 1 shows the Mask attack algorithm designed for image classification tasks.

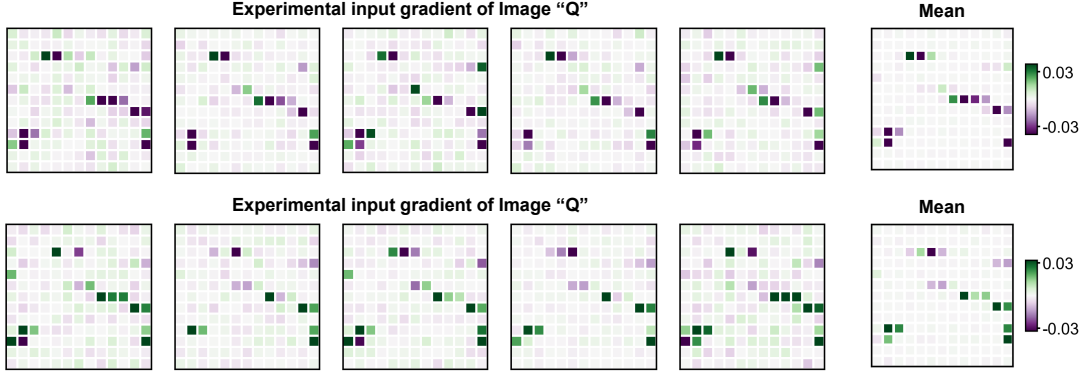


FIG. S6. **Experimental results of the input gradients for EMNIST.** The figures show the experimental input gradients measured for five distinct handwritten letter images (“Q” and “T”), and the mean input gradient averaged across 20 different images.

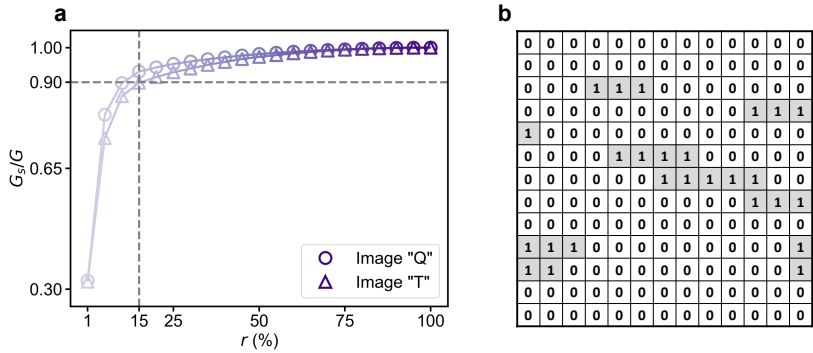
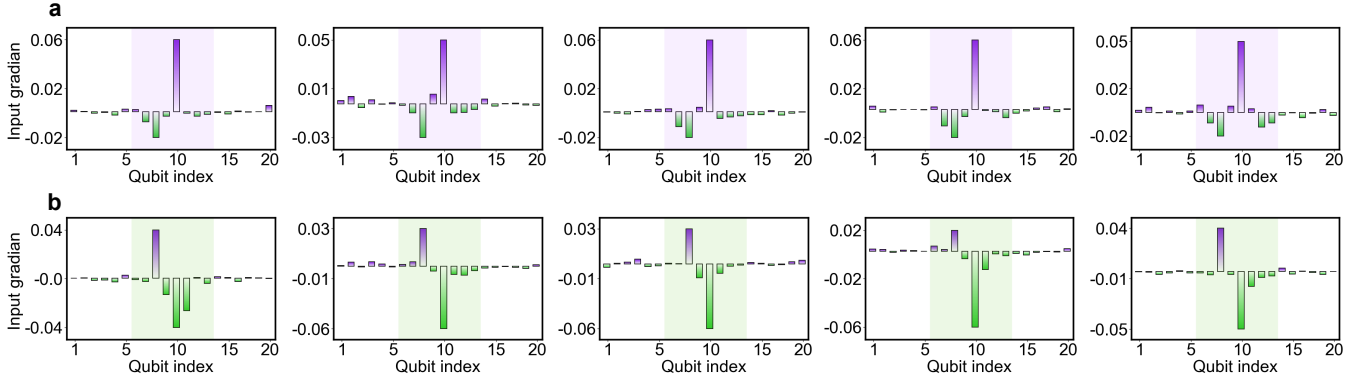


FIG. S7. **Mask  $\mathcal{M}$  construction based on experimental gradient sparsity for EMNIST.** **a.** Gradient magnitude proportion  $G_r/G$  as a function of pixel proportion, illustrating that the top 15% of pixels yield approximately 90% of the total gradient magnitude. **b.** The binary mask  $\mathcal{M}$  used in EMNIST experiments, where the elements corresponding to the top 15% of pixels are assigned 1, and all other positions are assigned 0.

Similarly, for the LCEI experiment, we analyzed the gradients of the rotation angles  $\alpha$  for all 20  $R_x$  gates, as shown in Fig. S8. Different cluster state samples exhibit comparable input gradient features, with gradient components predominantly concentrated on qubits Q7 to Q14. Accordingly, we performed localized attacks by perturbing the  $\alpha$  of these qubits. Algorithm 2 shows the Mask attack algorithm designed for cluster state excitation identification.



**FIG. S8. Experimental input gradients for LCEI.** The figures show the experimental input gradients for five distinct non-excited (a) and excited cluster states (b). Significant gradient components corresponding to rotation angles are observed on the central qubits (Q7 – Q14), which are highlighted with purple and green backgrounds. Each panel shows the average results obtained from 5 experimental repetitions.

---

**Algorithm 1** Mask FSGM of QNN classifier for EMNIST dataset

---

**Input:** A well-trained QNN classifier with parameters  $\theta^*$ , the loss function  $\mathcal{L}$ , the step size of the perturbation  $\epsilon$ , the binary mask vector  $\mathcal{M} = (m_1, m_2, \dots, m_n)^T$ , and a legitimate image  $\mathbf{x} = (x_1, x_2, \dots, x_n)^T$  with label  $c$ .

**Output:** The adversarial image  $\mathbf{x}'$

- 1: Initialization:  $\mathbf{x}' \leftarrow \mathbf{x}$ ,  $\delta \leftarrow \mathbf{0}$
- 2: **for**  $i \in [n]$  **do**
- 3:   **if**  $m_i = 1$  **then**
- 4:     Calculate the gradients of loss  $\mathcal{L}$  with respect to component  $x_i$ :  $\frac{\partial \mathcal{L}(f(\mathbf{x}; \theta^*), c)}{\partial x_i}$
- 5:     Generate perturbation:  $\delta_i \leftarrow \epsilon \cdot \text{sgn} \left[ \frac{\partial \mathcal{L}(f(\mathbf{x}; \theta^*), c)}{\partial x_i} \right]$
- 6:     Updates:  $x'_i \leftarrow x_i + \delta_i$
- 7:   **end if**
- 8: **end for**
- 9: **return**  $\mathbf{x}'$

---

**Algorithm 2** Mask FSGM of QNN classifier for LCEI

---

**Input:** A well-trained QNN classifier with parameters  $\theta^*$ , the loss function  $\mathcal{L}$ , the step size of the perturbation  $\epsilon$ , the binary mask vector  $\mathcal{M} = (m_1, m_2, \dots, m_n)^T$ , a legitimate  $n$ -qubits linear cluster state  $\rho_{\text{in}}$  with the rotation angle vector  $\alpha$  of  $R_x$  gates, and label  $c$ .

**Output:** The adversarial quantum state  $\rho'_{\text{in}}$  and corresponding rotation angle vector  $\alpha'$

- 1: Initialization:  $\alpha' \leftarrow \alpha$ ,  $\delta \leftarrow \mathbf{0}$
- 2: **for**  $i \in [n]$  **do**
- 3:   **if**  $m_i = 1$  **then**
- 4:     Calculate the gradients of loss  $\mathcal{L}$  with respect to angle  $\alpha_i$ :  $\frac{\partial \mathcal{L}(f(\rho_{\text{in}}; \theta^*), c)}{\partial \alpha_i}$
- 5:     Generate perturbation:  $\delta_i \leftarrow \epsilon \cdot \text{sgn} \left[ \frac{\partial \mathcal{L}(y(\rho_{\text{in}}; \theta^*), c)}{\partial \alpha_i} \right]$
- 6:     Updates:  $\alpha'_i \leftarrow \alpha_i + \delta_i$
- 7:   **end if**
- 8: **end for**
- 9: **return**  $\rho'_{\text{in}}$  and  $\alpha'$

---

**QUANTUM ROBUSTNESS ADVANTAGE INDUCED BY QUANTUM NOISE**

In this section, we theoretically investigate how quantum noise enhances the robustness of QNN classifiers. We revisit the definition of the adversarial robustness score, setting the normalized perturbation  $\hat{\epsilon} = 1$  for analytical convenience:

$$R_{\text{adv}} = \frac{1}{1 + \exp(\Delta p)}. \quad (\text{S15})$$

Here,  $\Delta p$  denotes the change in output probability induced by the perturbation  $\delta$  added to the input. We first consider the  $R_{\text{adv}}$  under ideal, noiseless conditions. Let  $\rho$  and  $\sigma$  represent the output qubit's density matrices corresponding to legitimate and

adversarial inputs, respectively. For the binary classification:

$$\rho = \begin{pmatrix} \rho_{00} & \rho_{01} \\ \rho_{10} & \rho_{11} \end{pmatrix}, \quad \sigma = \begin{pmatrix} \sigma_{00} & \sigma_{01} \\ \sigma_{10} & \sigma_{11} \end{pmatrix}. \quad (\text{S16})$$

We measure the output qubit in the computational basis  $\{|0\rangle, |1\rangle\}$  of the output qubit, with the measurement operator  $\mathcal{O}_k = |k\rangle\langle k|$ . Assuming the correct class corresponds to outcome  $|0\rangle$ , the probability of this outcome for a state  $\rho$  is  $p = \text{Tr}(\mathcal{O}_0\rho)$ , therefore:

$$\Delta p = \text{Tr}(\mathcal{O}_0\rho) - \text{Tr}(\mathcal{O}_0\sigma) = \rho_{00} - \sigma_{00}. \quad (\text{S17})$$

We now incorporate the effects of quantum noise over a circuit execution time  $t$ . We consider two primary types:  $T_1$  noise, characterizing energy relaxation and modeled by the amplitude damping channel:

$$\mathcal{E}_{\text{AD}}(\rho) = \begin{pmatrix} \rho_{00} + \rho_{11}(1 - e^{-t/T_1}) & \rho_{01}e^{-t/(2T_1)} \\ \rho_{10}e^{-t/(2T_1)} & \rho_{11}e^{-t/T_1} \end{pmatrix}, \quad (\text{S18})$$

and  $T_2$  noise, representing dephasing and corresponding to the phase damping channel:

$$\mathcal{E}_{\text{PD}}(\rho) = \begin{pmatrix} \rho_{00} & \rho_{01}e^{-t/(2T_2)} \\ \rho_{10}e^{-t/(2T_2)} & \rho_{11} \end{pmatrix}. \quad (\text{S19})$$

Assuming that amplitude damping and phase damping act independently, the composite noise channel applied to the output state is given by the concatenation  $\mathcal{E}_{\text{AD}} \circ \mathcal{E}_{\text{PD}}(\rho)$ , and the resulting noisy output density matrix:

$$\rho^{\text{noise}} = \mathcal{E}_{\text{AD}} \circ \mathcal{E}_{\text{PD}}(\rho) = \begin{pmatrix} \rho_{00} + \rho_{11}(1 - e^{-t/T_1}) & \rho_{01}e^{-t/(2T_1+2T_2)} \\ \rho_{10}e^{-t/(2T_1+2T_2)} & \rho_{11}e^{-t/T_1} \end{pmatrix}. \quad (\text{S20})$$

Consequently, evaluating the change in probability in the presence of noise:

$$\begin{aligned} \Delta p^{\text{noise}} &= (\rho_{00} + \rho_{11}(1 - e^{-t/T_1})) - (\sigma_{00} + \sigma_{11}(1 - e^{-t/T_1})) \\ &= (\sigma_{00} - \rho_{00}) + (\sigma_{11} - \rho_{11})(1 - e^{-t/T_1}) \\ &= (\sigma_{00} - \rho_{00}) - (\sigma_{00} - \rho_{00})(1 - e^{-t/T_1}) \\ &= \Delta p_k e^{-t/T_1}. \end{aligned} \quad (\text{S21})$$

Thus, the noisy change in probability is scaled by the factor  $e^{-t/T_1}$  compared to the noiseless case. The adversarial robustness score in the presence of noise is then:

$$R_{\text{adv}}^{\text{noise}} = \frac{1}{1 + \exp(e^{-t/T_1} \Delta p)}. \quad (\text{S22})$$

As a result,  $T_1$  noise mitigates the QNN's sensitivity to perturbations through the factor  $e^{-t/T_1}$  when measuring in the computational basis, thereby enhancing  $R_{\text{adv}}$ .

We extend our adversarial robustness results for noisy conditions to arbitrary measurement bases  $\{|\psi_+\rangle, |\psi_-\rangle\}$ , with the measurement operator  $\mathcal{O}_\psi = |\psi\rangle\langle\psi|$ . Such a basis can be expressed in terms of the computational basis:

$$|\psi_+\rangle = \alpha|0\rangle + \beta|1\rangle, \quad |\psi_-\rangle = \alpha^*|0\rangle - \beta^*|1\rangle, \quad (\text{S23})$$

with normalization condition  $|\alpha|^2 + |\beta|^2 = 1$ . Assuming the correct class corresponds to  $|\psi_+\rangle$ , the probability of this outcome for a state  $\rho$ :

$$\begin{aligned} p &= \text{Tr}(\mathcal{O}_{\psi_+}\rho) = \text{Tr}\left(\begin{pmatrix} |\alpha|^2 & \alpha\beta^* \\ \alpha^*\beta & |\beta|^2 \end{pmatrix} \begin{pmatrix} \rho_{00} & \rho_{01} \\ \rho_{10} & \rho_{11} \end{pmatrix}\right) \\ &= \rho_{00}|\alpha|^2 + \rho_{01}\alpha^*\beta + \rho_{10}\alpha\beta^* + \rho_{11}|\beta|^2, \\ &= \rho_{00}|\alpha|^2 + \rho_{11}|\beta|^2 + 2[\text{Re}(\rho_{01})\text{Re}(\alpha^*\beta) + \text{Im}(\rho_{01})\text{Im}(\alpha^*\beta)]. \end{aligned} \quad (\text{S24})$$

Therefore, we have

$$\Delta p = \text{Tr}(\mathcal{O}_{\psi_+}\rho) - \text{Tr}(\mathcal{O}_{\psi_+}\sigma) = \Delta\rho_{00}(|\alpha|^2 - |\beta|^2) + 2[\text{Re}(\Delta\rho_{01})\text{Re}(\alpha^*\beta) + \text{Im}(\Delta\rho_{01})\text{Im}(\alpha^*\beta)], \quad (\text{S25})$$

where  $\Delta\rho_{ij} = \rho_{ij} - \sigma_{ij}$ . We can express  $\Delta p$  as the sum of two components,  $A$  and  $B$ :

$$\begin{aligned} A &= \Delta\rho_{00}(|\alpha|^2 - |\beta|^2), \\ B &= 2 [\operatorname{Re}(\Delta\rho_{01}) \operatorname{Re}(\alpha^* \beta) + \operatorname{Im}(\Delta\rho_{01}) \operatorname{Im}(\alpha^* \beta)], \\ \Delta p &= A + B. \end{aligned} \quad (\text{S26})$$

Similarly, the probability change in the presence of noise:

$$\Delta p^{\text{noise}} = e^{-t/T_1} A + e^{-t/(2T_1+2T_2)} B, \quad (\text{S27})$$

This equation shows that for arbitrary measurement bases, the perturbation-induced change in output is jointly influenced by both  $T_1$  and  $T_2$  through different decay factors affecting components  $A$  and  $B$ . The overall impact of noise on  $R_{\text{adv}}$  thus depends on the specific measurement basis coefficients ( $\alpha$  and  $\beta$ ). For instance, when measuring in the Hadamard basis  $\{|+\rangle, |-\rangle\}$ , the adversarial robustness:

$$R_{\text{adv}}^{\text{noise}} = \frac{1}{1 + \exp(e^{-t/(2T_1+2T_2)} \Delta p)}. \quad (\text{S28})$$

## ROBUSTNESS BOUND OF QNN CLASSIFIER

Robustness bound represents the minimum perturbation distance between this legitimate sample and a perturbed sample that causes the classifier's prediction to change. This bound quantifies the classifier's ability to maintain correct predictions when subjected to a certain perturbation for a specific instance. Solving for the optimal robustness bound for each individual sample is generally computationally challenging. Therefore, two common approaches are employed to evaluate a classifier's robustness bounds: proving a theoretical lower bound or estimating an upper bound by constructing an effective attack. In this work, for quantum classifiers, we define robustness lower and upper bounds based on infidelity as the distance measure. Specifically, for a legitimate state  $\rho$ :

**Definition 1** (Robustness lower bound).  $R_{\text{LB}}$  is a robustness lower bound of  $\rho$  if there is no adversarial example when perturbed states  $\sigma$  satisfied  $D(\rho, \sigma) < R_{\text{LB}}$ .

**Definition 2** (Robustness upper bound).  $R_{\text{UB}}$  is a robustness upper bound of  $\rho$  if there exists at least one adversarial example when perturbed states  $\sigma$  satisfy  $D(\rho, \sigma) > R_{\text{UB}}$ .

In the main text, we present a method for extracting the robustness upper bound through adversarial attacks. Here, we provide the proof for the robustness lower bound given in Eq. (4). We begin by considering the vectors  $\mathbf{p}$  and  $\mathbf{q}$  with components  $\sqrt{p_k}$  and  $\sqrt{q_k}$ , where  $p_k = \operatorname{tr}(\Pi_k \rho)$  and  $q_k = \operatorname{tr}(\Pi_k \sigma)$  are the probabilities of measurement outcome for states  $\rho$  and  $\sigma$  respectively. The inner product defined as  $\mathbf{p} \cdot \mathbf{q} = \sum_k \sqrt{p_k q_k}$ , is related to the quantum fidelity  $F(\sigma, \rho)$ . According to quantum measurement theory, this relationship is governed by the inequality:

$$\mathbf{p} \cdot \mathbf{q} = \sum_k \sqrt{p_k q_k} \geq \sqrt{F(\rho, \sigma)}, \quad (\text{S29})$$

To derive the robustness lower bound, we seek the maximum possible value of the inner product  $\mathbf{p} \cdot \mathbf{q}$  when the state  $\sigma$  is just classified incorrectly. Assuming the elements of vector  $\mathbf{p}$  are sorted in descending order (i.e.  $p_1 > p_2 > \dots > p_n$ ), this task can be formulated as the following optimization problem:

$$\begin{aligned} &\max. \mathbf{p} \cdot \mathbf{q} \\ &\text{s.t. } \|\mathbf{q}\|_2 = 1 \\ &\quad \prod_{i=2}^n (q_1 - q_i) = 0, \end{aligned} \quad (\text{S30})$$

where  $\prod_{i=2}^n (q_1 - q_i) = 0$  ensures  $q_1 = q_i$  for some  $i \geq 2$ , reflecting the misclassification threshold. That is, misclassification occurs when the probability of the true class is no longer strictly greater than all other class probabilities. Applying the Lagrange multiplier method to solve this constrained optimization, as detailed in Ref. [24], yields the optimal value at the threshold where  $q_1 = q_2$ :

$$V^* = \sqrt{1 - \frac{1}{2}(\sqrt{p_1} - \sqrt{p_2})^2}, \quad (\text{S31})$$

where  $p_1$  and  $p_2$  are the largest and second largest elements of  $\mathbf{p}$ , respectively, and  $V^*$  denotes the maximum inner product under the misclassification constraint.

From this, we infer that if  $D(\rho, \sigma) < \frac{1}{2}(\sqrt{p_1} - \sqrt{p_2})^2$ , then  $\sqrt{F(\rho, \sigma)} > V^*$ . According to the Eq. (S29), having  $\mathbf{p} \cdot \mathbf{q} > V^*$  guarantees that the distribution  $\mathbf{q}$  must lie outside the misclassified region. This ensures that the perturbed state  $\sigma$  is always correctly classified, thereby defining the robustness lower bound as  $R_{\text{LB}} = \frac{1}{2}(\sqrt{p_1} - \sqrt{p_2})^2$ .

## QUANTUM PROCESSOR

### Device information

Our experiment was executed on a 72-qubit superconducting processor, featuring a  $6 \times 12$  arrangement of transmon qubits in a 2D lattice, divided into 12 frequency-multiplexed readout groups. Qubits are dispersively coupled to their dedicated readout resonator, which then shares a common readout input line in each frequency-multiplexed readout group. Each qubit exhibits a nonlinearity of around  $-240$  MHz, with individual microwave and flux lines for driving excitations and tuning its resonance frequency between  $|0\rangle$  and  $|1\rangle$ . We designed two types of qubits with different tunable frequency ranges: high-frequency qubits with a maximum frequency of  $4.8$  GHz, and low-frequency qubits being  $4.4$  GHz. The processor includes 126 tunable couplers, enabling adjustable effective coupling strength between neighboring qubits with a maximum of  $-40$  MHz. Each coupler is also a transmon qubit, controlled by a single flux line for frequency tuning across a range of approximately  $4$  to  $6.5$  GHz. Due to fabrication defects, including Josephson junction shorts and internal wire breaks within the packaging box, five qubits and four couplers on our processor are non-functional.

For the experiment, we selected 20 qubits, denoted as  $Q_i$ , where  $i = 1, 2, \dots, 20$ , showing in Fig. S9. Their maximum frequencies and the readout resonator frequencies are shown in Fig. S10a and e. The energy relaxation ( $T_1$ ) times and the Ramsey dephasing ( $T_2^*$ ) times measured at the working frequency are shown in Fig. S10c and d. Average characteristic parameters of these 20 qubits are listed in Table S1.

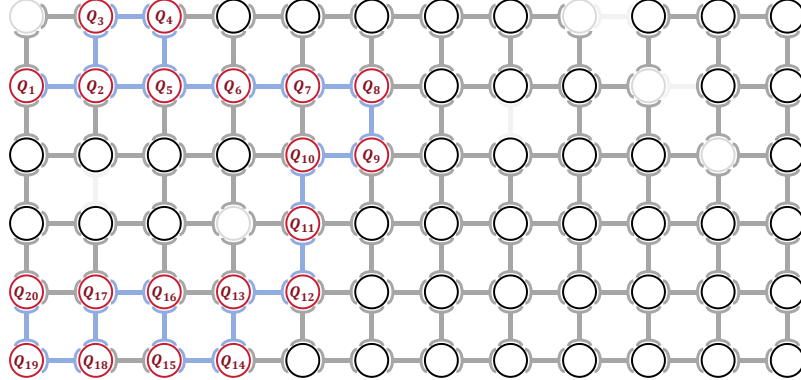


FIG. S9. **Layout of our 72-qubit superconducting processor.** The 20 qubits and the adjacent couplers used in our experiment are shown in red and blue, respectively. The unworked qubits and couplers are marked with a light gray colour.

Our superconducting quantum processor is fabricated using flip-chip technology, with all qubits and couplers located on the top chip, control/readout lines and readout resonators situated on the bottom chip. The two chip substrates are physically and electrically interconnected via indium bumps: by precisely aligning the two chips and performing thermocompression bonding, the chips are firmly joined together via the bumps, resulting in a completed flip-chip device. Additionally, a niobium airbridge process is implemented on the chip to suppress parasitic slotline modes in the coplanar waveguides, thereby reducing electromagnetic crosstalk between different control lines. Following chip fabrication, the processor is packaged within a silver-plated aluminum sample box for electromagnetic shielding. Qubit control lines are wire-bonded to one end of PCB strips, with the other end connected to external SMP RF coaxial connectors.

### Experimental setup

The quantum processor is installed in a dilution refrigerator (DR) and cooled to a base temperature of  $15$  mK. Each qubit has two control lines: the XY line for qubit driving and the Z control line for biasing the qubit to its working point. Each coupler has

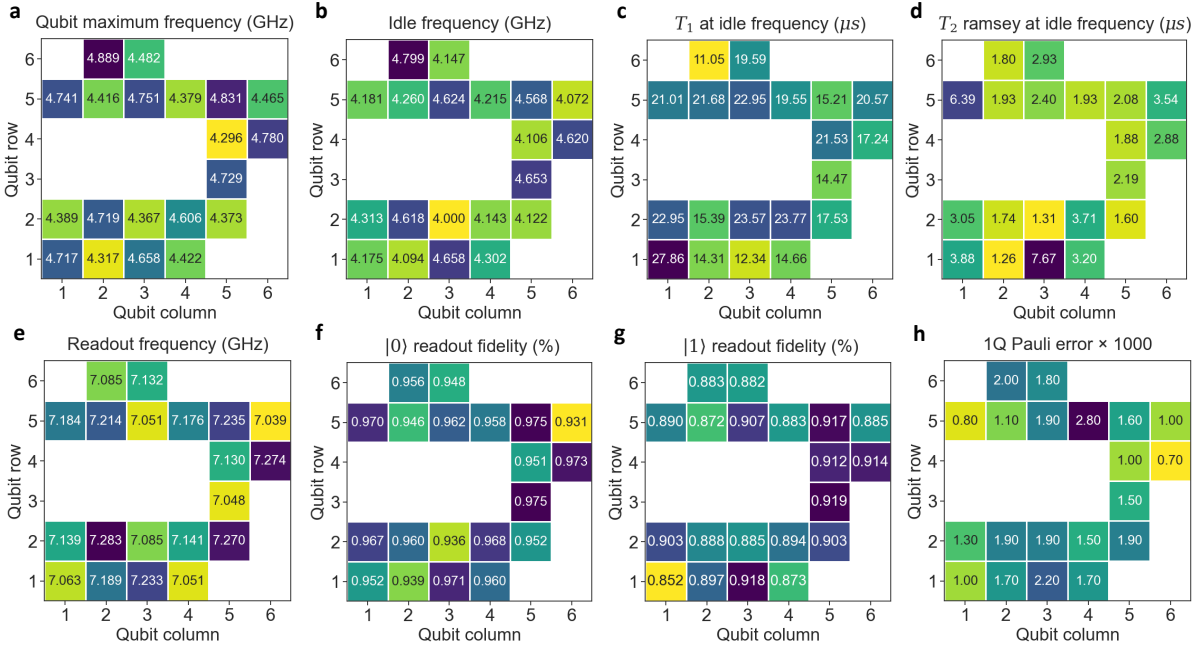


FIG. S10. **Heatmaps of various single-qubit parameters.** **a** and **b**, Qubit maximum frequency and working frequencies. **c** and **d**, Qubit relaxation and dephasing time is measured at working frequencies. **e**, Readout resonator frequencies. **f** and **g**, Simultaneous readout fidelity when qubits are prepared at  $|0\rangle$  and  $|1\rangle$ . **h**, Single-qubit Pauli error characterized by simultaneous XEB experiment.

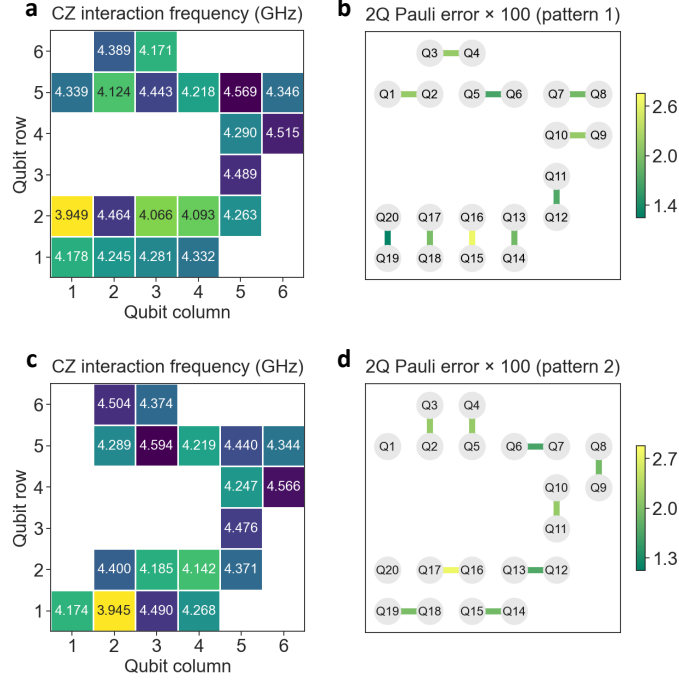


FIG. S11. **Heatmaps of CZ gate parameters.** **a** and **c**, Simultaneous CZ gate interaction frequencies. **b** and **d**, Two-qubit Pauli error characterized by simultaneous 2Q-XEB experiment.

one Z control line. Waveform generation is based on custom arbitrary waveform generator (AWG) modules. Each AWG module provides 8 DACs with a 14-bit resolution, providing sampling rates of 3.2 GS/s for XY-pulses and 1.2 GS/s for Z-pulses. The bias signals and fast Z-pulse for qubits and couplers are directly output by the AWG. Single-qubit XY drive and measurement microwave pulses are synthesized by mixing the AWG output with a local oscillator (LO) signal, producing signals with arbitrary spectral content within a  $\pm 250$  MHz bandwidth. For qubit state readout, the input measurement microwave is delivered to the

TABLE S1. System parameters for our quantum processor.

Parameters	Median	Mean	Stdev.	Units
Qubit maximum frequency	4.544	4.566	0.187	GHz
Qubit working frequency	4.237	4.333	0.244	GHz
Qubit anharmonicity	-0.237	-0.232	0.017	GHz
Readout resonator frequency	7.140	7.151	0.080	GHz
Readout linewidth $\kappa/2\pi$	1.07	1.17	0.43	MHz
Dispersive shift $\chi/2\pi$	1.15	1.14	0.21	MHz
Readout fidelity of $ 0\rangle$	0.959	0.958	0.013	%
Readout fidelity of $ 1\rangle$	0.891	0.893	0.017	%
$T_1$ at working frequency	19.57	18.86	4.33	$\mu$ s
$T_2$ Ramsey at working frequency	2.29	2.86	1.59	$\mu$ s
Simultaneous 1Q Pauli error	0.17	0.16	0.05	%
Individual 2Q Pauli error	1.92	1.91	0.42	%
Simultaneous 2Q Pauli error (pattern 1)	1.98	1.99	0.40	%
Simultaneous 2Q Pauli error (pattern 2)	1.98	1.90	0.52	%

quantum processor through the readout line, and the output signal passes through three circulators before being amplified by an impedance-matched parametric amplifier (IMPA). Then, it passes through a fourth circulator and undergoes further amplification at 4K and room temperature by high electron mobility transistor (HEMT) amplifiers. Finally, the amplified signal is sampled and processed by room-temperature electronics.

Within the DR, attenuators and filters are strategically installed at different stages to minimize noise. To suppress thermal noise from higher temperature stages, the XY control lines, Z control lines, and readout input lines incorporate a total attenuation of 40 dB, 23 dB, and 60 dB, respectively. Additionally, all XY control lines are equipped with 6 GHz low-pass filters, while Z control lines utilize 500 MHz low-pass filters. DC-blocks are also installed on all XY and readout input lines. To minimize noise introduced through the IMPA control lines, each IMPA pump line is equipped with a 20 dB attenuator and 12.2  $\sim$  14 GHz band-pass filter. Each IMPA bias line is equipped with a 20 dB attenuator and RC filter. The simplified wiring diagram is shown in Fig. S12.

## DEVICE CONTROL CALIBRATION

### Calibration procedure

As the number of qubits in a quantum processor increases, calibration becomes increasingly challenging. Traditional one-by-one calibration schemes are time-consuming and lack scalability. More importantly, particularly as parameter drift in both qubits and room-temperature electronics limits the feasibility of prolonged calibration procedures. While the tunability of qubit and coupler frequencies offers flexibility in selecting parameters for single- and two-qubit gates, it also complicates the determination of working frequencies.

Here, we briefly introduce our calibration strategy. We define key operational frequencies: the maximum transition frequency of a qubit as the “sweet point”, the single-qubit gate operating frequency as the “working point”, and the CZ gate operating frequency as the “interaction point”. The calibration process for our processor is structured into five stages: pre-calibration, spectroscopy testing, frequency allocation, fine calibration, and CZ gate calibration.

To characterize the processor efficiently before determining working frequencies, we prioritize parallel calibration while minimizing crosstalk and residual coupling. During spectroscopy testing, we group the qubits according to the following frequency constraints: (1) The frequency difference between nearest-neighbor qubits,  $\Delta f_{NN}$ , satisfies  $|\Delta f_{NN}| \geq 300$  MHz. (2) The frequency difference between next-nearest-neighboring qubits,  $\Delta f_{NNN}$ , satisfies either  $\alpha - 60$  MHz  $\geq |\Delta f_{NNN}| \geq 60$  MHz or  $|\Delta f_{NNN}| \geq \alpha + 60$  MHz, where  $\alpha$  is the qubit anharmonicity. Qubits within the same group can be calibrated in parallel, enhancing efficiency. The specific experiments for each calibration stage are detailed below:

- Pre-calibration. This stage establishes the fundamental parameters of the IMPA and readout resonators: (1) Finding the working point for optimal gain and bandwidth. (2) Determining the frequency of each qubit’s readout resonator. (3) Measuring the readout resonator frequency as a function of the qubit flux bias. (4) Measuring the readout resonator frequency of the nearest neighbor qubit as a function of the coupler flux bias.
- Spectroscopy testing. Spectroscopy testing begins by biasing all couplers to their maximum frequency as determined in

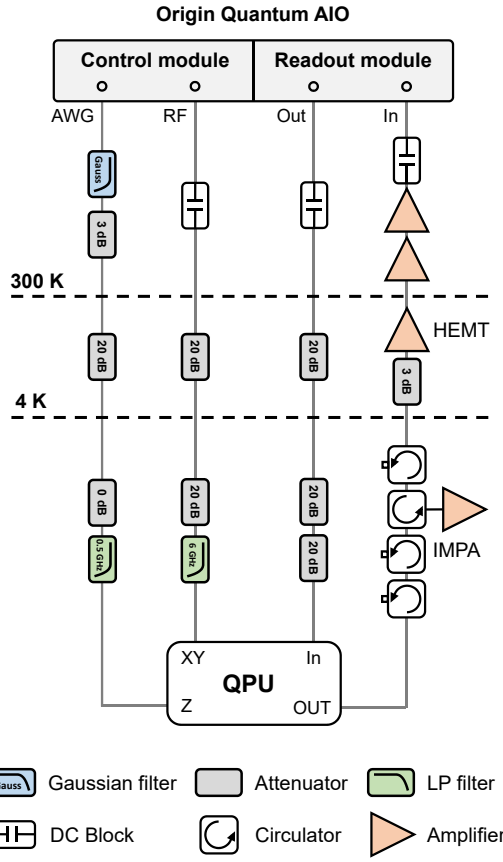


FIG. S12. Experimental schematic of simplified quantum processor control and readout wiring.

pre-calibration, followed by a coarse calibration of single-qubit gates at the sweet point in a grouped parallel manner. This includes: (1) Identifying each qubit's transition frequency. (2) Calibrating the pulse amplitude for  $X_\pi$  and  $X_{\pi/2}$  gates. (3) Measuring and aligning the relative timing between the XY and Z control lines. (4) Evaluating microwave crosstalk between different qubit control lines. Subsequently, by varying the Z-pulse amplitude, we sample  $T_1$ ,  $T_2$ , and randomized benchmarking (RB) fidelity across each qubit's frequency range. These measurements inform the subsequent frequency allocation.

- Frequency allocation. For working frequency allocation, we use a uniform error model to describe the overall error rate  $e_{\text{total}}$  for parallel single-qubit gate execution. This model is weighted by factors including  $T_1$ ,  $T_2$ , XY crosstalk, and residual ZZ coupling, and is expressed as  $e_{\text{total}} = \sum_i w_i e_i(f_{\text{working}})$ . For interaction frequency allocation, additional factors such as Z signal distortion and spectator qubit effects are considered. The frequency allocation employs an open-loop optimization algorithm, starting with a central qubit and iteratively optimizing the frequency pattern while calculating the error rate  $e_{\text{total}}^{(t)}$  for gates executed in parallel within a 2-distance neighborhood. The optimal frequency allocation from the  $t$ -th iteration constrains the  $t + 1$ -th iteration, aiming to minimize the overall error rate. The final working frequency and interaction frequency for the 20 qubits are shown in Fig. S10b and Fig. S11.
- Fine calibration. Following frequency allocation, all couplers are biased to the frequency minimizing ZZ coupling, and all qubits are set to their working frequencies for parallel fine calibration of single-qubit gates. This stage includes DRAG pulse parameter optimization and readout fidelity optimization (adjusting the frequency and amplitude of readout pulses and qubit readout frequency). The single-qubit gate performance measured by simultaneous cross-entropy benchmarking (XEB), shown in Fig. S10h.
- CZ gate calibration. This stage involves preparatory steps: (1) Correction of Z-pulse distortion for both qubits and couplers. (2) Measuring and aligning the relative timing between Z control lines for qubit-qubit and qubit-coupler. Subsequently, CZ gate parameters are calibrated to ensure high-fidelity two-qubit operations, with details provided in the CZ gate calibration section.

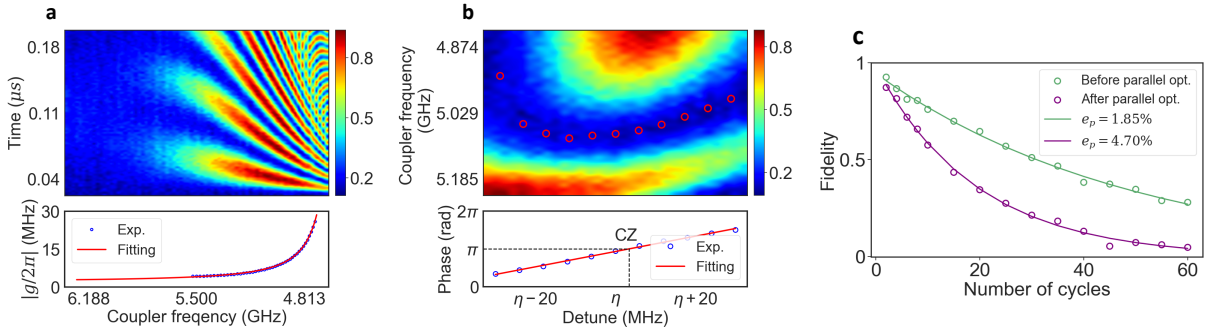


FIG. S13. **Characterization of the parameters of the CZ gate.** **a**, Two-qubit swap experiment shows that the effective coupling strength of the neighboring qubits can be dynamically tuned by biasing the middle coupler. **b**, The top panel shows the probability of preparing  $|Q_1Q_2\rangle$  in state  $|11\rangle$  and after the interaction state  $|20\rangle$ , we mark the coupler frequency and the detuning of  $|Q_1Q_2\rangle$  corresponding to the minimum leakage with red circles. The bottom panel shows the measured controlled phase under the parameters corresponding to the red circles in the top panel, where the black dashed line gives the point when the phase is  $\pi$ .  $\eta$  denotes anharmonicity. **c**, After parallel optimization by the Nelder-Mead algorithm, the error of the parallel two-qubit gates extracted by the simultaneous 2Q-XEB experiments is significantly reduced.

### CZ gate calibration

We implement the CZ gate as a coupling-tunable diabatic gate, where the effective coupling strength between  $Q_1$  and  $Q_2$  arises from both direct coupling and the contribution mediated by a tunable coupler. This can be rapidly tuned by controlling the coupler frequency, the effective coupling strength can be expressed as:

$$\tilde{g} = \frac{1}{2} \left( \frac{1}{\Delta_1} + \frac{1}{\Delta_2} - \frac{1}{\Sigma_1} - \frac{1}{\Sigma_2} \right) g_{1,c} g_{2,c} + g_{1,2}, \quad (\text{S32})$$

where  $\Delta_i = \omega_i - \omega_c$ ,  $\Sigma_i = \omega_i + \omega_c$  and  $g_{i,j}$  is the direct coupling between qubits or couplers. In the Fig. S13a, we measure the SWAP dynamics in the  $|11\rangle \rightleftharpoons |20\rangle$  resonance versus the coupler frequency, demonstrating that the effective coupling strength can be continuously tuned within the range of  $-30$  MHz.

To execute the CZ gate, we apply a fast Z-pulse to the coupler's control line, tuning it from the coupling-off point to an effective coupling strength of  $|g/2\pi| \approx 14$  MHz. Simultaneously, we bias  $Q_1$  and  $Q_2$  from their working frequency to the interaction frequencies, where  $|101\rangle$  and  $|200\rangle$  are in near resonance (with  $Q_2$  at a lower frequency). After a period of non-adiabatic interaction, this yields a two-qubit gate equivalent to a CZ gate (up to a single-qubit phase factor). To minimize rising-edge distortion at the nanosecond scale, CZ pulses for both the qubits and the coupler employ flattop Gaussian waveforms, defined as:

$$z(t) = \frac{A}{2} \left( \text{erf} \left( \frac{t - \tau_b}{\sqrt{2}\sigma} \right) - \text{erf} \left( \frac{t - \tau_b - \tau_c}{\sqrt{2}\sigma} \right) \right), \quad (\text{S33})$$

where  $A$  is the amplitude of the Z-pulse,  $\sigma$  controls the Gaussian smoothing of the rising edge,  $\tau_c$  is the effective pulse width, and  $\text{tau}_b$  is the buffer at both ends of the effective pulse. The total width of the CZ pulse is  $t_{\text{total}} = \tau_c + 2\tau_b$ . In the experiment, we set  $t_{\text{total}} = 40$  ns,  $\sigma = 1.25$  and  $\tau_b = 7.5$ , leaving the parameters of the CZ pulse amplitude  $A$  for qubits and coupler to be determined through calibration. Our calibration procedure for the CZ gate is as follows:

- First, we determine the amplitude of the CZ pulse by sweeping the coupler's Z-pulse amplitude while varying the detuning  $\Delta$  between  $|101\rangle$  and  $|200\rangle$ . This identifies the trajectory that minimizes state leakage, corresponding to the coupler frequency that maximizes the  $|1\rangle$  population of  $Q_2$ . In Fig. S13b, red circles represent the fitted coupler frequency from experimental results as a function of detuning ( $f_{\text{coupler}}(\Delta)$ ) at the minimum leakage. We determine the Z-pulse amplitudes of the qubits and coupler in the Control-phase (CPHASE) gate by  $f_{\text{coupler}}(\Delta)$ .
- Next, we optimize the controlled phase by measuring the controlled phase at various detunings. We initialize  $Q_1$  in  $|0\rangle$  and  $|1\rangle$ , apply the CPHASE pulse, and perform quantum state tomography (QST). As shown by the blue circles in Fig. S13b, the controlled phase varies continuously within  $[0, 2\pi]$  as a function of detuning. By linearly fitting points near  $\pi$ , we extract the precise pulse amplitude for the CZ gate. Subsequently, we applied a virtual Z gate to compensate for the unwanted single-qubit phase accumulated during the CZ pulse.

- For parallel CZ gate optimization, we execute a 2Q-XEB experiment with a fixed depth, using the population of the final state as the objective function. Parameters optimized include the qubits' interaction frequencies, the coupler's Z-pulse amplitude, and single-qubit phases, aiming to minimize crosstalk between control lines. The Nelder-Mead (NM) algorithm is employed for optimization. As shown in Fig. S13c, this significantly reduces the simultaneous two-qubit Pauli error. The Pauli errors for all 19 pairs of two-qubit gates, measured via simultaneous XEB, are presented in Fig. S11b and d.

### Readout error mitigation

To correct measurement errors, we adopt the iterative Bayesian unfolding (IBU) method [49], which addresses the limitations of traditional matrix inversion techniques, such as negative probability entries and amplified statistical uncertainties. For  $n$  qubits, we define a  $2^n \times 2^n$  assignment matrix  $R$  that maps the ideal probability distribution on the measurement basis to a noisy probability distribution, where  $R_{ij} = \Pr(\text{meas.} = j | \text{prep.} = i)$  represents the conditional probability of measuring state  $j$  given preparation state  $i$ .  $R$  can be constructed by single-shot experiments on  $n$  qubits, assuming negligible readout crosstalk. Single-shot readout fidelities of the experimental 20 qubits are shown in Fig. S10f and g. Given the noise probability distribution  $w$ , IBU iteratively computes the corrected distribution  $v$  as:

$$v_j^{(t+1)} = \sum_i^{2^n} \frac{w_i R_{ij} v_j^{(t)}}{\sum_j R_{jk} v_j^{(t)}}, \quad (\text{S34})$$

where  $t$  is the number of iterations, and  $v^{(0)}$  is the initial guess, typically chosen to be a uniform distribution. In our experiments, the maximum number of iterations is set to 50.